An Analysis of Coordinated Observations from NOAA's *Ronald H. Brown* Ship and G-IV Aircraft in a Landfalling Atmospheric River over the North Pacific during CalWater-2015

PAUL J. NEIMAN,[a] NATALIE GAGGINI,[b] CHRISTOPHER W. FAIRALL,[a] JOSHUA AIKINS,[c]
J. RYAN SPACKMAN,[b,f] L. RUBY LEUNG,[d] JIWEN FAN,[d] JOSEPH HARDIN,[d]
NICHOLAS R. NALLI,[e] AND ALLEN B. WHITE[a]

[a] *Physical Sciences Division, NOAA/Earth System Research Laboratory, Boulder, Colorado*
[b] *Science and Technology Corporation, and NOAA/Earth System Research Laboratory, Boulder, Colorado*
[c] *Cooperative Institute for Research in the Environmental Sciences, and NOAA/Earth System Research Laboratory, Boulder, Colorado*
[d] *Pacific Northwest National Laboratory, Richland, Washington*
[e] *I. M. Systems Group, NOAA/NESDIS/STAR, College Park, Maryland*

ABSTRACT

To gain a more complete observational understanding of atmospheric rivers (ARs) over the data-sparse open ocean, a diverse suite of mobile observing platforms deployed on NOAA's R/V *Ronald H. Brown* (*RHB*) and G-IV research aircraft during the CalWater-2015 field campaign was used to describe the structure and evolution of a long-lived AR modulated by six frontal waves over the northeastern Pacific during 20–25 January 2015. Satellite observations and reanalysis diagnostics provided synoptic-scale context, illustrating the warm, moist southwesterly airstream within the quasi-stationary AR situated between an upper-level trough and ridge. The AR remained offshore of the U.S. West Coast but made landfall across British Columbia where heavy precipitation fell. A total of 47 rawinsondes launched from the *RHB* provided a comprehensive thermodynamic and kinematic depiction of the AR, including uniquely documenting an upward intrusion of strong water vapor transport in the low-level moist southwesterly flow during the passage of frontal waves 2–6. A collocated 1290-MHz wind profiler showed an abrupt frontal transition from southwesterly to northerly flow below 1 km MSL coinciding with the tail end of AR conditions. Shipborne radar and disdrometer observations in the AR uniquely captured key microphysical characteristics of shallow warm rain, convection, and deep mixed-phase precipitation. Novel observations of sea surface fluxes in a midlatitude AR documented persistent ocean surface evaporation and sensible heat transfer into the ocean. The G-IV aircraft flew directly over the ship, with dropsonde and radar spatial analyses complementing the temporal depictions of the AR from the *RHB*. The AR characteristics varied, depending on the location of the cross section relative to the frontal waves.

1. Introduction

To better understand the physical processes driving extreme winter precipitation and the variability of water supply across flood- and drought-prone California, a broad multiyear, interagency, multiplatform observing initiative called CalWater was devised and is being carried out (Ralph et al. 2016). The primary targets of this ongoing campaign are atmospheric rivers (ARs) and atmospheric aerosols. ARs are long and narrow corridors of strong lower-tropospheric water vapor transport in the warm sector of extratropical cyclones (e.g., Zhu and Newell 1998; Ralph et al. 2004). Landfalling ARs are often accompanied by heavy precipitation (e.g., Dettinger 2004; Stohl et al. 2008; Neiman et al. 2008a,b, 2014a, 2016; Smith et al. 2010; Viale and Nuñez 2011; Ralph et al. 2011; Ralph and Dettinger 2012; Lavers and Villarini 2013) that can yield profound hydrometeorological impacts, including lower-altitude flooding (e.g., Dettinger 2004; Ralph et al. 2003, 2006, 2011; Dettinger et al. 2011; Lavers et al. 2011; Neiman et al. 2011) and an increase in high-elevation mountain snowpack (e.g., Neiman et al. 2008b; Guan et al. 2012, 2013). Aerosols, which originate from both local sources and via long-range transport, can modulate the intensity and distribution of precipitation during AR landfalls (e.g.,

[f] Current affiliation: NASA Ames Research Center, Earth Science Division, Moffett Field, California.

Corresponding author: Paul J. Neiman, paul.j.neiman@noaa.gov

Ault et al. 2011; Creamean et al. 2013, 2015). Collecting and analyzing extensive CalWater measurements in the AR environment of landfalling winter storms—such as was done in this study—is motivated by gaining a more complete observational understanding of ARs over data-sparse oceanic regions, with the ultimate goal of reducing uncertainties in weather forecasts and climate projections during extreme precipitation events that can yield both beneficial and destructive effects.

Initial field-phase activities during the winters of 2009–11 compose what is now called CalWater1. The primary foci of CalWater1 research included the impacts of aerosols on precipitation during landfalling ARs (Ault et al. 2011; Creamean et al. 2013, 2015), the interaction between ARs and the Sierra barrier jet (e.g., Kingsmill et al. 2013; Neiman et al. 2013a; White et al. 2015), and the microphysical characteristics of precipitation (White et al. 2015). To fill remaining science gaps, a follow-on set of winter field experiments—collectively called CalWater2—commenced in 2014, with added emphasis on research aircraft interrogation of ARs over the data-sparse Pacific Ocean offshore of the U.S. West Coast. Although the CalWater-2014 campaign was limited in scope relative to 2015 and 2016 activities because only a single aircraft was available, it was instrumental in furthering CalWater's objectives. An airborne-centric observational study by Neiman et al. (2016) documented multiple transient frontal waves in the AR environment offshore. These waves propagated across northern California and generated periods of heavy orographically enhanced rainfall when the AR impacted the state's coastal and inland mountains, as captured by a ground-based suite of instruments from the National Oceanic and Atmospheric Administration (NOAA)'s Hydrometeorology Testbed (HMT; hmt.noaa.gov) program (Ralph et al. 2013; White et al. 2013).

The winter of 2015 represented the first major field season for CalWater2, during which four research aircraft operated by three government agencies and deployed from California and Hawaii flew more than 50 missions over the Pacific, while the NOAA Research Vessel (R/V) *Ronald H. Brown* (*RHB*) conducted a major research cruise from Hawaii to California. The overarching motivation for the *RHB* cruise was to provide unique marine and atmospheric observations over the open ocean to study processes associated with extreme precipitation during the landfall of ARs over the steep topography of western North America. In addition, the existing ground-based HMT observing network was augmented with a National Science Foundation–supported site for aerosols and microphysics. Finally, in coordination with the observing facilities described above, the U.S. Department of Energy's (DOE) Atmospheric Radiation Measurement (ARM) program sponsored and executed the ARM Cloud Aerosol and Precipitation Experiment (ACAPEX; Leung 2016; Ralph et al. 2016). Combined, these observing platforms provided unique marine and atmospheric observations of ARs over the open ocean and at landfall.

Many previous AR studies have used information provided by microwave instruments on satellites to document the vertically integrated water vapor evolution of ARs over the oceans and the overland impacts of ARs (e.g., Ralph et al. 2004; Neiman et al. 2008b, 2011; among others). A subset of AR studies also had the benefit of episodic dropsonde deployments from different types of research aircraft during AR-focused field campaigns to better document the horizontal and vertical structure of ARs (e.g., Ralph et al. 2004; Neiman et al. 2016; Wick et al. 2017, manuscript submitted to *J. Atmos. Oceanic Technol.*). The current study expands upon previous AR research by presenting comprehensive analyses that also include a temporally continuous set of in situ and remote sensing observations from the *RHB* far from the influence of the continental terrain. During CalWater-2015, the *RHB* was instrumented with a DOE mobile observing facility, a rawinsonde system, and NOAA's air–sea flux system that provided continuous flux observations (see section 2). These multiday flux observations were especially unique, providing the first-of-their-kind time series within a long-duration AR over the open ocean on 20–25 January 2015 that ultimately made landfall and produced heavy rainfall and localized flooding for a 5-day period across western British Columbia. Together with dropsonde and radar data from two NOAA G-IV research flights that were coordinated with the unique *RHB* assets, we are able to describe with unprecedented detail the dynamic, thermodynamic, and microphysical structures of this long-duration AR, which possessed multiple mesoscale frontal waves over the data-sparse ocean.

Although the combined efforts of CalWater-2015, HMT, and ACAPEX provided a diverse suite of observing systems based in California, the state was experiencing a serious drought at the time because the storm track was diverted consistently northward by a persistent ridge along the U.S. West Coast. Hence, the strongest ARs remained well offshore of California during most of that winter, and they primarily impacted the Pacific Northwest and British Columbia instead. Fortunately, the ship and air resources aligned to provide the unprecedented observations for this study. Section 2 describes the observing systems and gridded datasets. Synoptic context is provided in section 3, while section 4 presents a mesoscale analysis of data collected

by the offshore observing platforms. Concluding thoughts are offered in section 5.

2. Observing systems and gridded datasets

The *RHB* was the cornerstone surface-based observing platform for CalWater-2015 (http://oceanexplorer.noaa.gov/technology/vessels/ronbrown/ronbrown.html). At 84 m in length, the *RHB* is the largest in NOAA's fleet. The ship departed Honolulu, Hawaii, on 14 January 2015 and proceeded northeastward, then northward, for ~5.5 days. It subsequently remained stationary at 38°N, 140°W from ~0900 UTC 20 January to 1500 UTC 25 January, which represents this study's primary period of interest. Thereafter, the *RHB* headed eastward, temporarily making port in San Francisco, California, on 29–30 January. The cruise eventually terminated in San Diego, California, on 10 February.

The *RHB* housed an impressive array of atmospheric and oceanographic instrumentation. Those systems that are relevant to this study are described here. RS92 Väisälä rawinsondes (Nalli et al. 2016) measured vertical profiles of pressure (± 1 hPa), wind velocity ($\pm 0.15\,\mathrm{m\,s^{-1}}$; $\pm 2°$), temperature ($\pm 0.2°$C), and relative humidity ($\pm 5\%$) at <6-m vertical resolution. A 1290-MHz wind profiler was installed by DOE's ACAPEX as part of their ARM Mobile Facility (AMF2; Martin et al. 2014). The wind profiler measured hourly averaged profiles of horizontal wind in a high mode (from 0.72 to 5.12 km MSL every ~75 m) and a low mode (from 0.29 to 2.60 km MSL every ~62 m). The data were edited objectively using the vertical–temporal continuity method of Weber et al. (1993) and were then inspected manually to look for and remove any remaining outliers. Sea clutter contamination rendered the profiler data largely unusable during the 6-day window, except after 1700 UTC 24 January. Another AMF2 asset included the vertically pointing Ka-band zenith radar (KAZR; Widener et al. 2012) that remotely probes clouds and light precipitation at a frequency of 35 GHz (i.e., $\lambda = 8.6$ mm). It collected reflectivity, vertical velocity, and spectral width data every 0.36 s with a range resolution of ~30 m from the surface to ~20 km MSL. A collocated Parsivel laser disdrometer (Löffler-Mang and Joss 2000) recorded raindrop size distributions and resulting estimates of the rain rate every 60 s. NOAA's Physical Sciences Division deployed and operated a near-surface meteorology system to measure pressure, temperature, relative humidity (at 0.1 Hz), and wind velocity (10 Hz, a sonic anemometer) on a jackstaff for best exposure to undistorted flow. The sonic anemometer and a collocated infrared absorption hygrometer provided 10-Hz time series of fluctuations in vertical velocity, temperature, and specific humidity. A sea snake sea surface temperature (SST) sensor was towed through the water at a depth of ~5 cm to gather data at 0.1 Hz. All data were averaged into 5-min blocks. Meteorological and SST data were used to calculate sea surface sensible and latent heat fluxes (H_S and H_L, respectively; see the appendix for details). Six rain gauges of varying types (i.e., bucket, optical, acoustic) measured rainfall; these data were averaged into 5-min blocks.

NOAA's G-IV research jet aircraft (www.omao.noaa.gov/learn/aircraft-operations/aircraft/gulfstream-iv-sp-g-iv) was another key observing platform for CalWater-2015 and collected atmospheric observations far offshore of California during two flights originating from McClellan Airfield in Sacramento. Flight 1 commenced at 2031 UTC 22 January 2015, released 12 dropsondes between 2254 UTC 22 January and 0140 UTC 23 January, and returned to base at 0338 UTC 23 January, while flight 2 took off at 1809 UTC 24 January, released 23 dropsondes between 2005 and 2303 UTC 24 January, and landed at 0033 UTC 25 January. The G-IV capabilities are described as in Neiman et al. (2016). The aircraft has a cruising altitude of ~13.5 km MSL and speed of ~230 m s⁻¹, a maximum range of ~7000 km, and eight dropsonde channels. The dropsondes use the Airborne Vertical Atmospheric Profiling System (www.eol.ucar.edu/isf/facilities/dropsonde) to measure vertical profiles of pressure (± 1 hPa), wind velocity ($\pm 0.5\,\mathrm{m\,s^{-1}}$), temperature ($\pm 0.2°$C), and relative humidity ($\pm 5\%$). Measurements are taken every ~0.5 s for the variables, corresponding to ~6-m vertical resolution near the surface. The G-IV was equipped with a tail Doppler radar (TDR) for measuring precipitation and wind velocities (J. F. Gamache, NOAA/AOML/Hurricane Research Division, 2015, personal communication). The TDR operates at an X-band frequency of 9.3 GHz (i.e., $\lambda = 3.2$ cm), scans 20° fore and aft of the fuselage's long axis, has a beamwidth of 2.7°, and an along-track resolution of 1125 m. Because of the large beamwidth, the TDR observations suffered from significant beam broadening. Hence, our TDR analyses are within about ± 40 km horizontal distance of the flight track. Ground clutter and sidelobe effects were manually removed to mitigate contamination in the lower troposphere. The decluttered data were then interpolated onto a Cartesian grid with 1.5-km horizontal and 0.5-km vertical resolution. We present TDR analyses from the second flight only.

As described previously in Neiman et al. (2016), integrated water vapor (IWV) and cloud liquid water (CLW) were retrieved from the Special Sensor Microwave Imager/Sounder (i.e., SSMIS; Kunkee et al. 2008) aboard the *F16*, *F17*, and *F18* polar-orbiting satellites. These retrievals (Wentz 1995; Karstens et al. 1994) are

confined to oceanic regions where surface emissivity is weak, and they have a native resolution of ~40 km in ~1700-km-wide swaths. They were placed on a ~25-km-resolution grid and combined into twice-daily composite images for the time intervals 0000–1159 UTC ("morning" or a.m.) and 1200–2359 UTC. This study uses the morning composites.

For synoptic-scale context, our study utilizes the Climate Forecast System Reanalysis (CFSR; Saha et al. 2010) gridded dataset from NOAA's National Centers for Environmental Prediction. This reanalysis package is available at 6-h time steps on a 0.5° latitude × 0.5° longitude grid with 37 vertical levels.

3. Synoptic-scale context

During the period of interest between 20 and 25 January 2015, an upper-level trough and ridge persisted over the central North Pacific Ocean and U.S. West Coast, respectively (not shown). Between these two synoptic-scale features, an AR embedded in baroclinic southwesterly flow and modulated by a series of transient frontal waves extended from the subtropics to British Columbia. A collection of morning SSMIS satellite images (Fig. 1) shows the evolution of the long, narrow AR plume from an IWV perspective. Initially, the AR was situated west of the *RHB* (Fig. 1a). Thereafter, the oscillating AR was positioned closer to the *RHB* (Figs. 1b–f). Six transient frontal waves are labeled in the IWV imagery, each corresponding to a comma feature and/or inflection associated with a short-wave trough at 500 hPa (not shown) migrating northeastward on the east side of the upper-level large-scale trough. Starting on 25 January (Fig. 1f), the AR began moving eastward across the *RHB* and subsequently dissipated in response to the eastward migration and weakening of the upper-level synoptic-scale trough (not shown). Companion SSMIS satellite imagery of CLW shows a well-defined linear and/or comma-shaped enhancement with each of the frontal waves (Fig. 2). These frontal waves remained largely west of the *RHB*, except on 25 January when wave 6 moved across the *RHB* during the final eastward-moving phase of the AR.

A set of CFSR analyses of vertically integrated horizontal water vapor transport [IVT; methodology as described in Neiman et al. (2008b)] between 1000 and 200 hPa at 1200 UTC 20–25 January 2015 is presented in Fig. 3. These analyses are ~6–10 h later than the corresponding SSMIS images on the same day. At 1200 UTC 20 January (Fig. 3a), a corridor of enhanced IVT marked the AR to the west of the *RHB*. One day later (Fig. 3b), the AR had moved eastward over the *RHB* with the passage of frontal wave 2. The subsequent frontal waves retained strong IVT within the quasi-stationary AR near the *RHB* until 1200 UTC 25 January (Figs. 3c–f). Thereafter, the vapor fluxes in the AR moved eastward and weakened markedly (not shown). During the 6-day period, the IVT analyses depict a poleward extension of tropical water vapor transport exceeding $250 \, \text{kg} \, \text{s}^{-1} \, \text{m}^{-1}$ into the AR in the south-central portion of the domain at 1200 UTC 23 January (Fig. 3d). No other analysis times contained a comparable tropical–midlatitude vapor transport linkage exceeding $250 \, \text{kg} \, \text{s}^{-1} \, \text{m}^{-1}$—either within the domain or to its southwest (not shown)—despite the fact that the IWV imagery suggested a poleward extrusion of tropical water vapor into the AR (Fig. 1). The downwind portion of the AR's vapor transport plume intermittently made landfall, primarily over British Columbia but also across Washington.

A corresponding six-panel image of 925-hPa geopotential height and equivalent potential temperature θ_e from the CFSR (Fig. 4) highlights the low-level atmospheric conditions. From 1200 UTC 20 to 24 January 2015 (Figs. 4a–e), a deep extratropical cyclone was situated over the North Pacific and a strong anticyclone persisted off the U.S. West Coast. Between the two, strong southwesterly flow in the AR advected high-θ_e air from the subtropics to the *RHB* and, ultimately, toward the British Columbia coast. During this period, each of the six frontal waves was tied to a transient low-level trough. By 1200 UTC 25 January (Fig. 4f), the deep North Pacific cyclone dissipated and a remnant trough was moving across the *RHB* toward the weakening West Coast anticyclone. This trough was accompanied by a wind shift from southwesterly in the high-θ_e AR airstream to northwesterly in the low-θ_e postfrontal airstream farther west.

Companion CFSR contour maps of the 0°C surface (i.e., the freezing level) are shown in Fig. 5. During the period, an enhanced freezing-level gradient persisted southwest through north of the *RHB*, marking the midtropospheric baroclinic transition between the cold synoptic-scale trough over the central North Pacific and warm air farther southeast in the AR. The freezing level above the *RHB* exceeded 3000 m MSL until after the passage of frontal wave 6 at 1200 UTC 25 January. Each frontal wave generated a poleward bulge with a locally higher freezing level, consistent with a warm-advection comma cloud head signature. With the landfall of each successive frontal wave in the persistent AR, the freezing level increased over western British Columbia, from ~1000 m MSL at 1200 UTC 20 January 2015 to ~3000 m MSL over the southwest portion of the province 5 days later. These high freezing levels are consistent with prior studies showing warmer-than-normal conditions in the

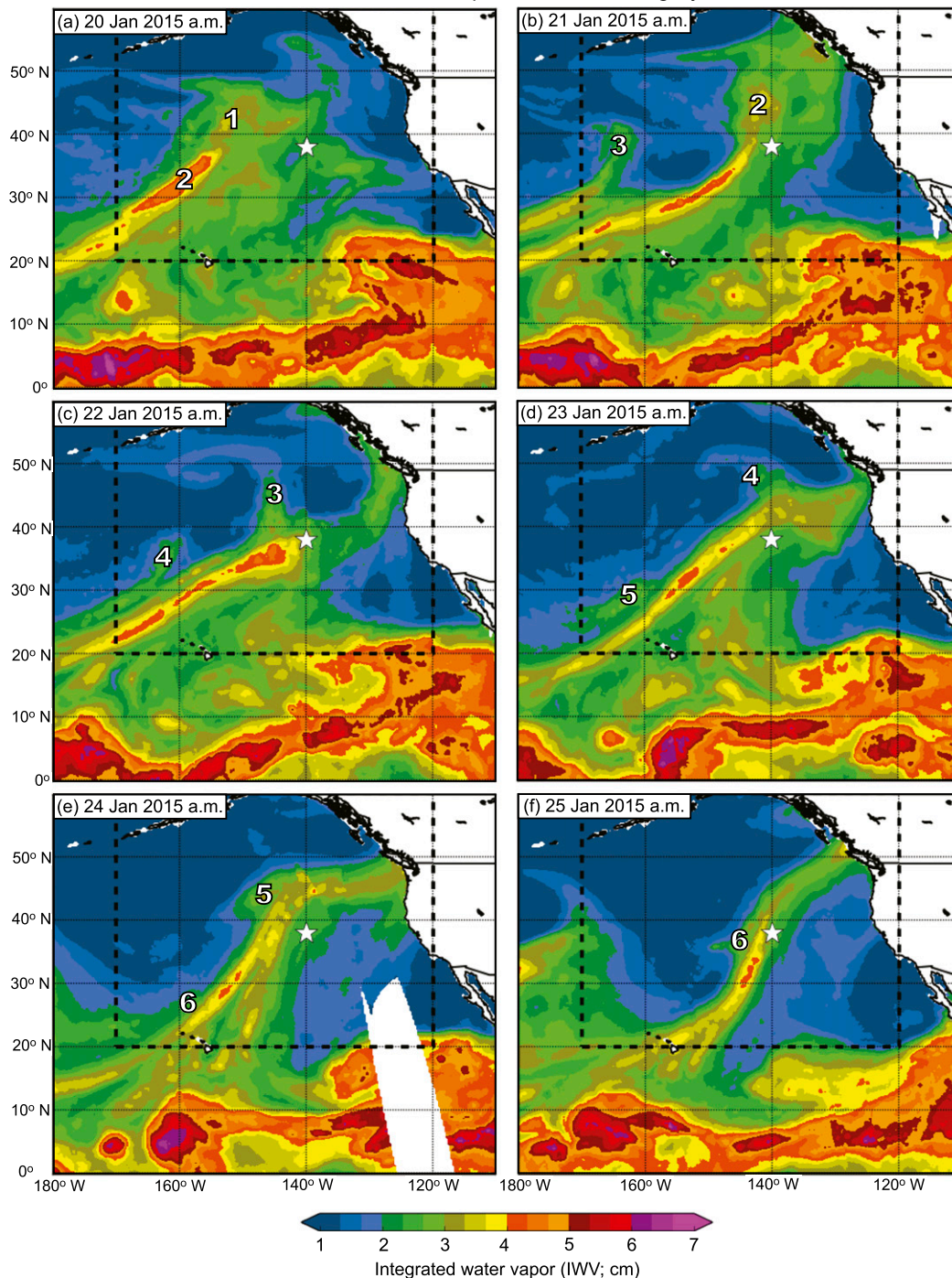SSMIS IWV composite satellite imagery

FIG. 1. (a)–(f) Composite SSMIS satellite imagery of IWV (cm; color scale) constructed from polar-orbiting swaths between 0000 and 1159 UTC (morning images) on 20–25 Jan 2015. White regions signify missing data. The dashed box in each panel shows the domain of the CFSR analyses in Figs. 3–5 and the satellite imagery in Fig. 10. The boldface numbers mark the six frontal waves described in the text. The white star denotes the position of the *RHB*.

SSMIS CLW composite satellite imagery
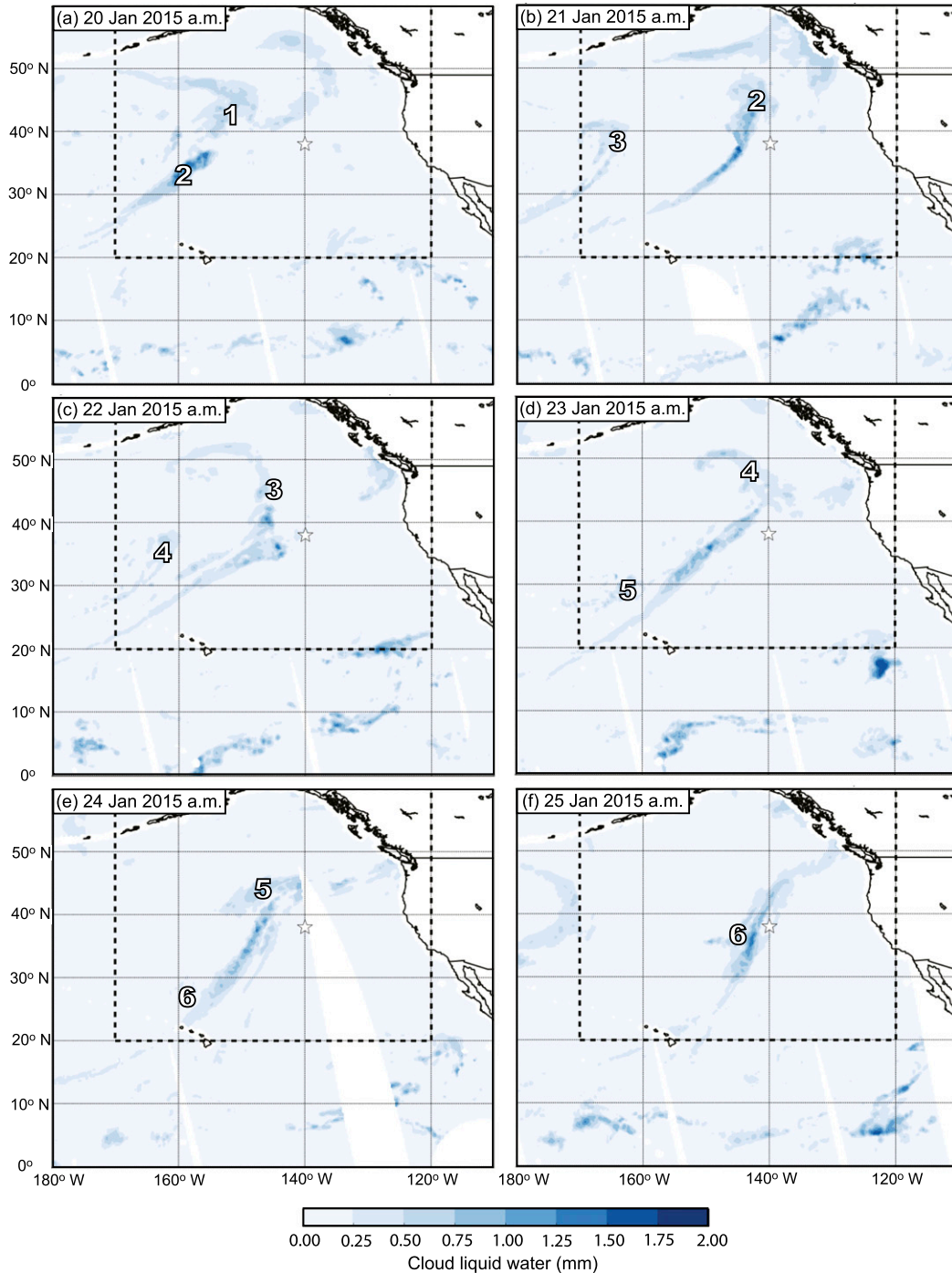
Fig. 2. As in Fig. 1, but for CLW (mm).

AR environment (e.g., Dettinger 2004; Neiman et al. 2008a,b, 2011).

During the roughly 5 days of landfalling AR conditions across British Columbia, the sustained onshore low-level flow and strong vapor fluxes maximized precipitation (~100–200 mm) in the orographically favored western portion of the province upwind of its highest terrain (not shown). These overland observations highlight the fact that orographic lift played a major role in concentrating the AR precipitation, as has been documented in previous
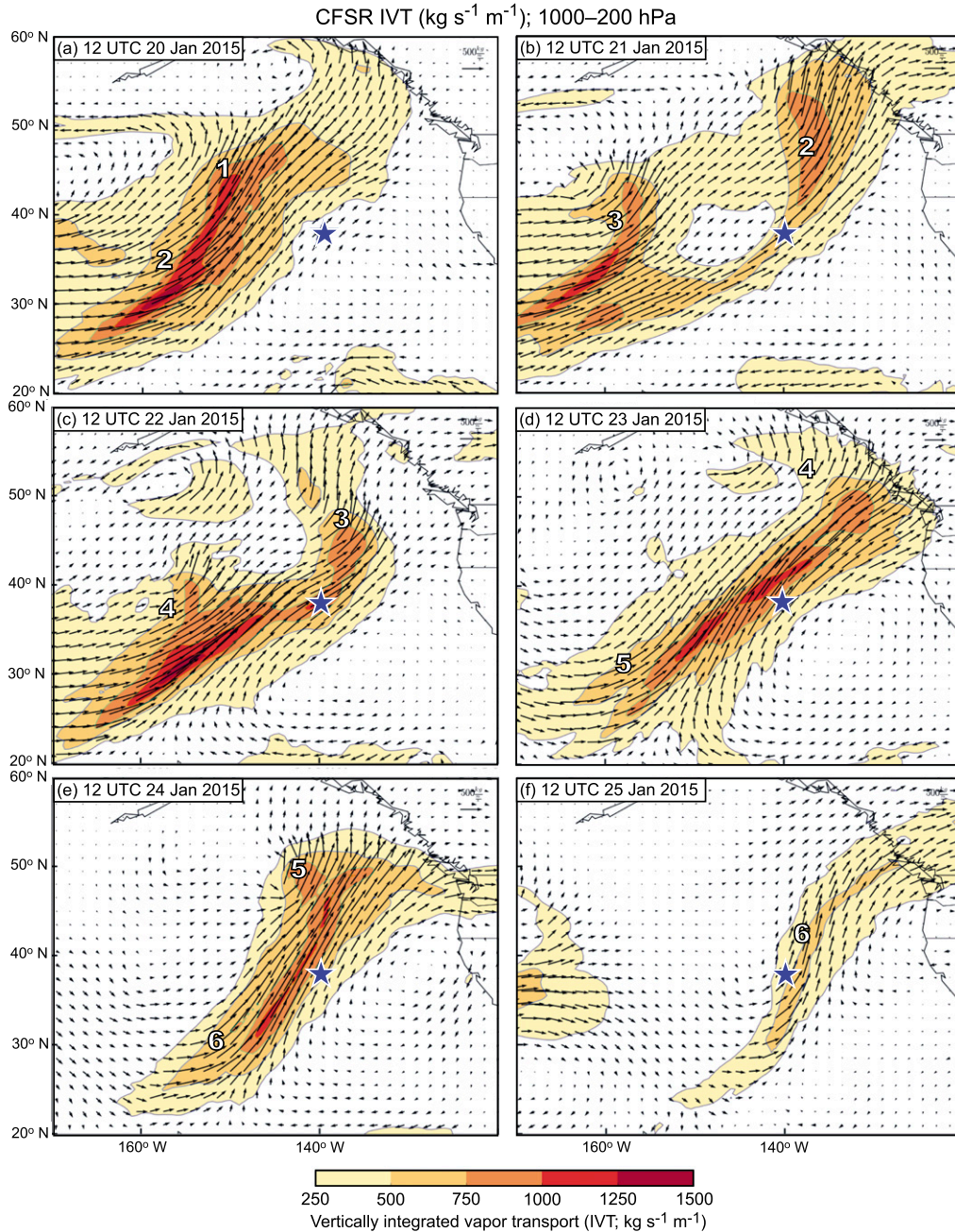
CFSR IVT (kg s^{-1} m^{-1}); 1000–200 hPa

FIG. 3. Plan-view analyses of the 1000–200-hPa IVT (kg s^{-1} m^{-1}; see magnitude color scale; vector size proportional to magnitude) from the 0.5° × 0.5° resolution CFSR dataset every 24 h between (a) 1200 UTC 20 Jan and (f) 1200 UTC 25 Jan 2015. The numbers mark the six frontal waves described in the text. The star in each panel denotes the position of the *RHB*.

studies (e.g., Dettinger 2004; Stohl et al. 2008; Nieman et al. 2008a,b, 2013a, 2014a,b, 2016; Smith et al. 2010; Viale and Nuñez 2011; Ralph et al. 2011; Ralph and Dettinger 2012; Lavers and Villarini 2013). As the freezing level increased with time over western British Columbia during persistent AR conditions, the areal fraction of the

mountain basins receiving rain rather than snow also increased, thus contributing to enhanced runoff and localized flooding region wide (not shown). Indeed, a combination of high freezing levels and heavy precipitation in earlier landfalling ARs have been shown to contribute to flooding (e.g., Dettinger 2004; Ralph et al.
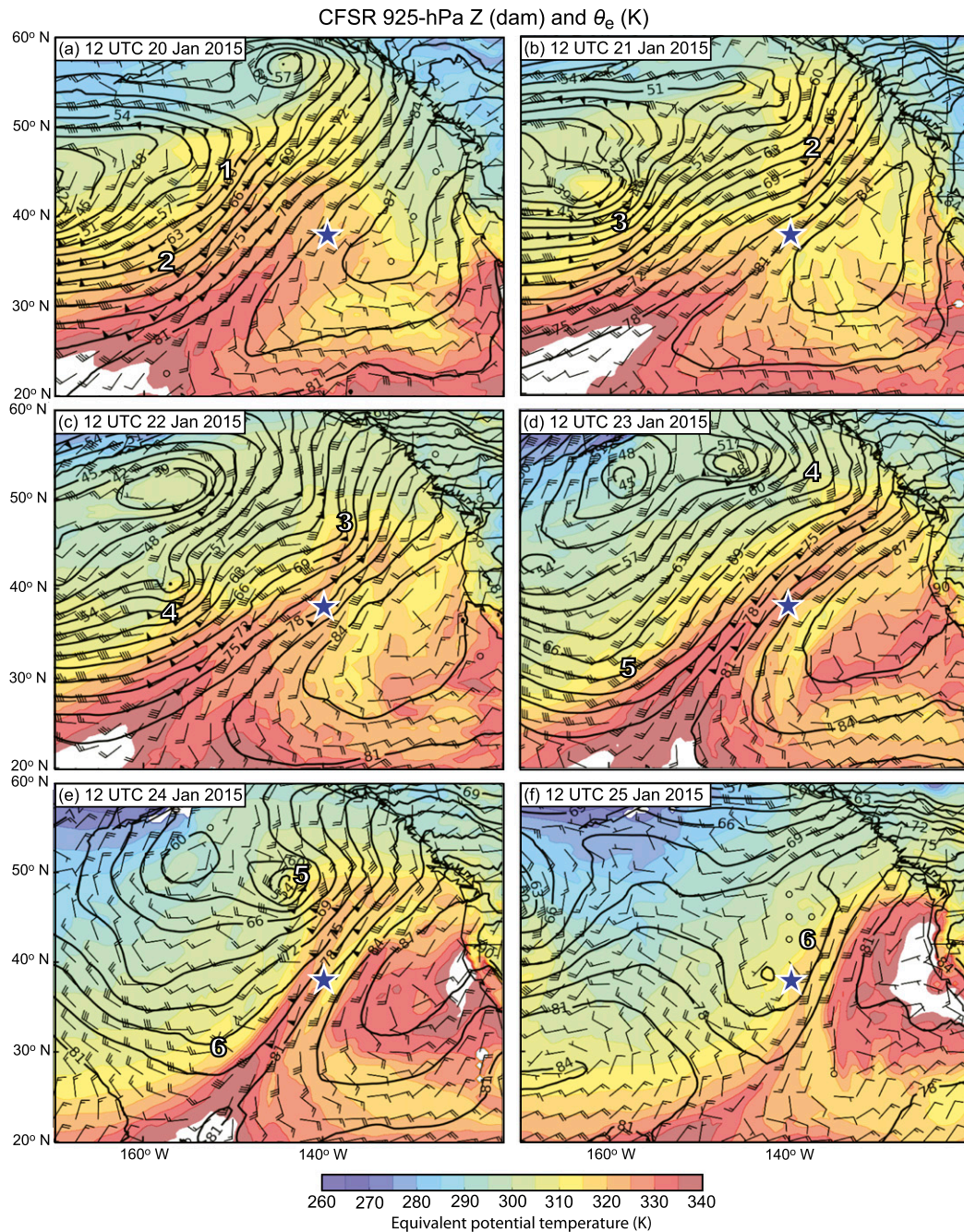
CFSR 925-hPa Z (dam) and θ_e (K)

FIG. 4. As in Fig. 3, but for 925-hPa geopotential height (dam; black contours), θ_e (K; see color scale), and wind velocities (flags, $25\,\mathrm{m\,s}^{-1}$; barbs, $5\,\mathrm{m\,s}^{-1}$; half-barbs, $2.5\,\mathrm{m\,s}^{-1}$).

2003, 2006, 2011; Dettinger et al. 2011; Lavers et al. 2011; Neiman et al. 2011, 2013b).

4. Multiplatform offshore mesoscale analysis

A diverse set of observing systems collected data on board the *RHB* and G-IV during the AR case study of

20–25 January 2015. Coordinated analyses of these data are presented in the following subsections.

a. NOAA R/V Ronald H. Brown

Forty-seven rawinsondes launched from the *RHB* between 0301 UTC 20 January and 2157 UTC 25 January provided a comprehensive 6-day time–height depiction of

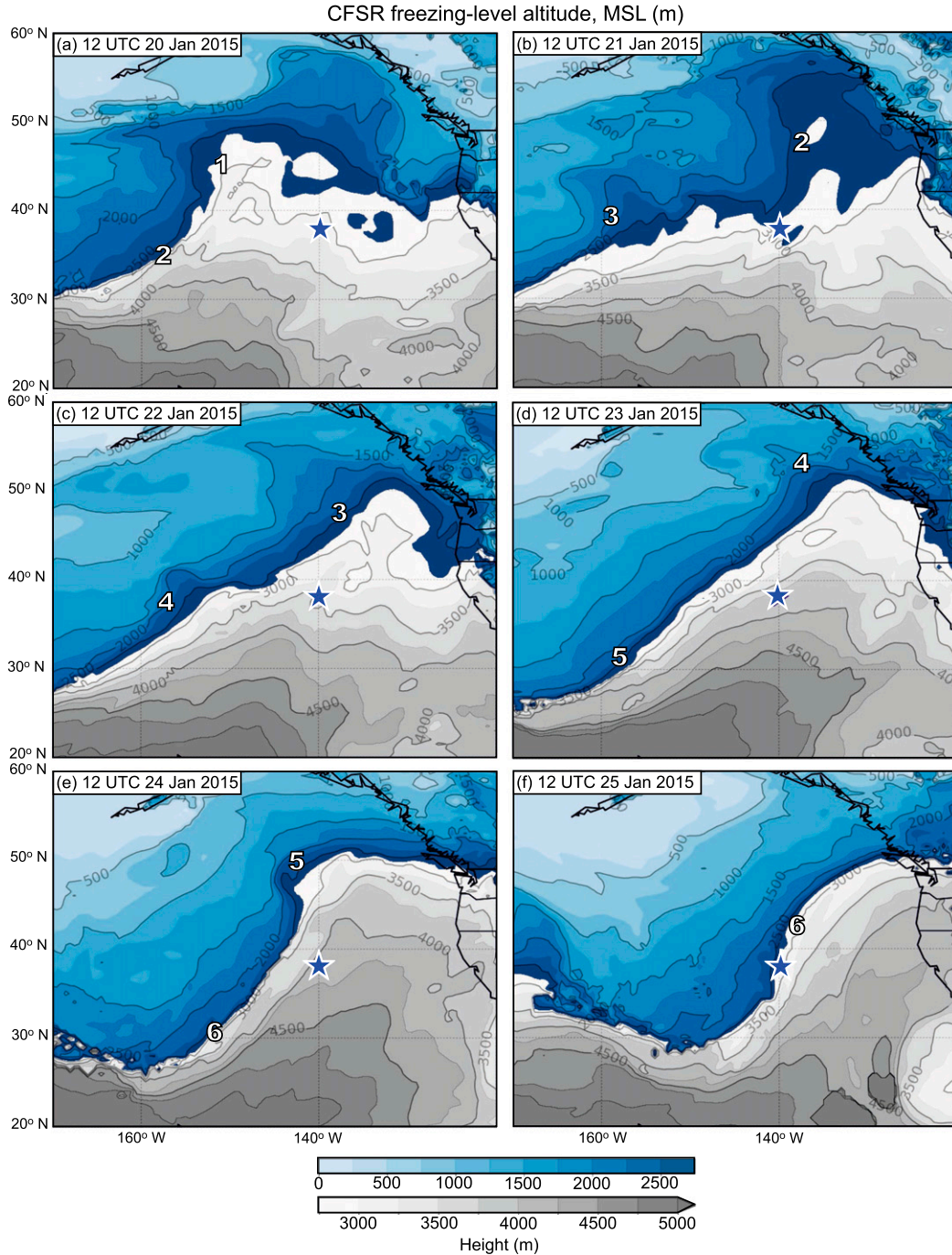CFSR freezing-level altitude, MSL (m)

FIG. 5. As in Fig. 3, but for the freezing-level altitude (m, MSL; color scale).

the atmospheric conditions within the persistent AR over the data-sparse North Pacific (Fig. 6; see also Nalli et al. 2016). The AR-parallel IVT (Fig. 6d) exceeded 250 kg m^{-1} s^{-1} between 1300 UTC 20 January and 1800 UTC 25 January. Prior studies have used this minimum vapor transport threshold to define ARs in reanalysis datasets, especially since AR plumes with IVT $\geq$ 250 kg m^{-1} s^{-1} often overlap with areas of heavy precipitation during landfall (e.g., Rutz et al. 2014; Neiman et al. 2013a, 2016). During this period, five well-defined peaks in IVT were observed, each exceeding 500 kg m^{-1} s^{-1}; they correspond to frontal waves 2–6 passing near or west of the *RHB* (frontal wave 1 was too far northwest of the *RHB* to be observed). Each peak coincided with a local maximum in IWV that far
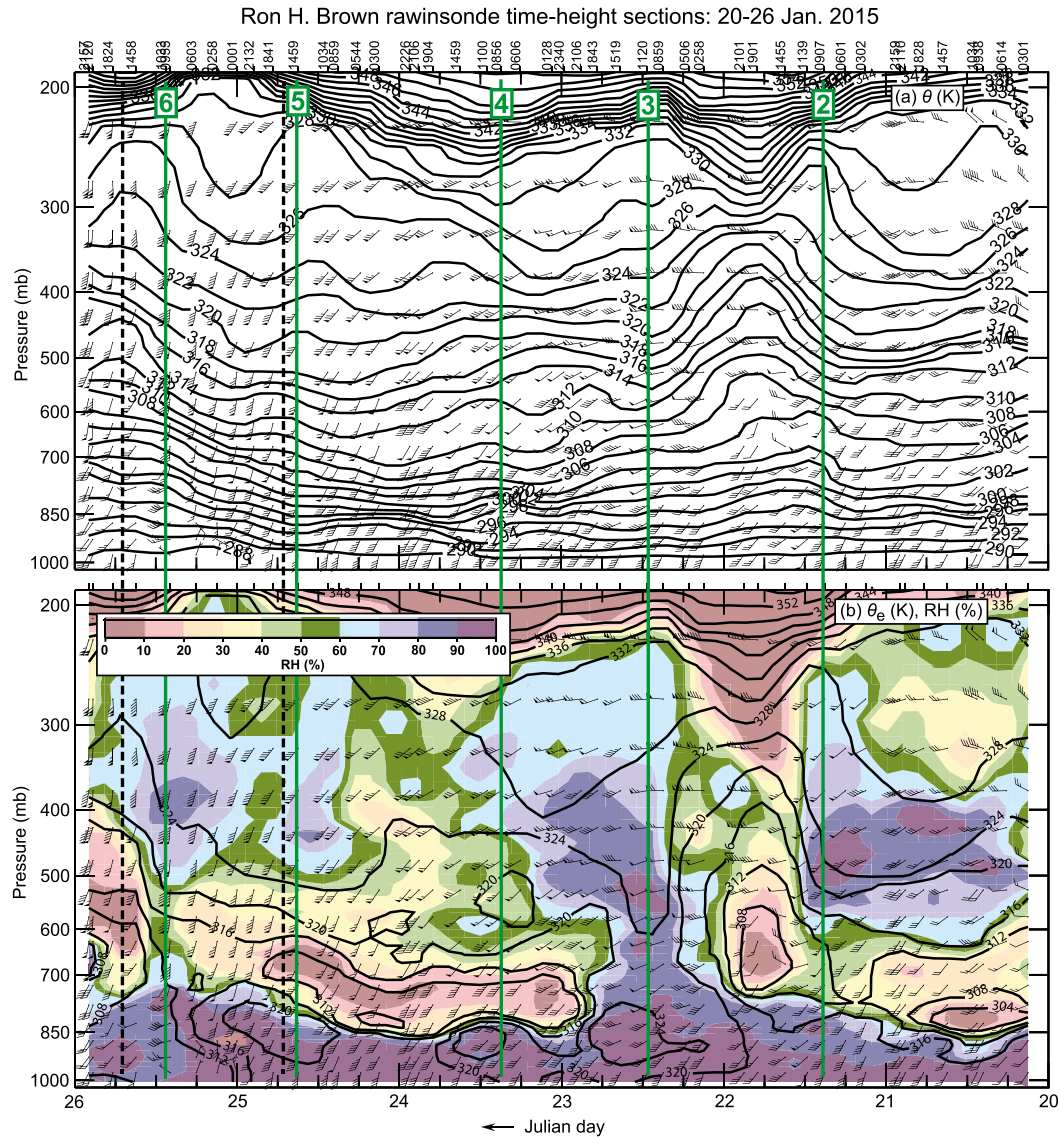
FIG. 6. Time–height analyses and vertically interpolated wind profiles (every 50 hPa; wind flags and barbs are as in Fig. 4) from rawinsondes released on the *RHB* between 0301 UTC 20 Jan and 2157 UTC 25 Jan 2015: (a) θ (K; black contours), (b) θ_e (K; black contours) and relative humidity (%; color scale), and (c) AR-parallel horizontal water vapor flux calculated in adjacent 50-hPa layers (kg s^{-1} m^{-1}; directed from 230°; black contours, with shading >50 kg s^{-1} m^{-1}). (d) Rawinsonde time series of 1000–200-hPa AR-parallel IVT (kg s^{-1} m^{-1}; solid) and IWV (cm; dashed). The pair of black dashed vertical lines highlights the temporal bounds of the *RHB* wind-profiler time–height and time series analyses in Figs. 8 and 9. The five green vertical lines mark the maximum IVT associated with frontal waves 2–6.

exceeded the minimum 2-cm threshold defined in Ralph et al. (2004) for AR conditions. In addition, sustained values of IWV > 2 cm coincided with the persistent AR values of IVT exceeding 250 kg s^{-1} m^{-1}. A companion cross section of vertically resolved AR-parallel vapor transport (VT; Fig. 6c) shows enhanced VT in persistent southwesterly flow, eventually weakening with the passage of an eastward-propagating front at ~2200 UTC 24 January that marked the onset of changing synoptic conditions.

Each IVT maximum (save the last and weakest one) was tied to an upward protrusion of VT that likely occurred in response to upward motion with the passage of the transient frontal waves. The deepest vertical penetration occurred with frontal wave 3 at 1120 UTC 22 January, when IVT reached 1000 kg m^{-1} s^{-1}.

Corresponding cross sections of potential temperature (θ; Fig. 6a) and θ_e with relative humidity (RH) (Fig. 6b) reveal cooling and drying aloft and a shift from

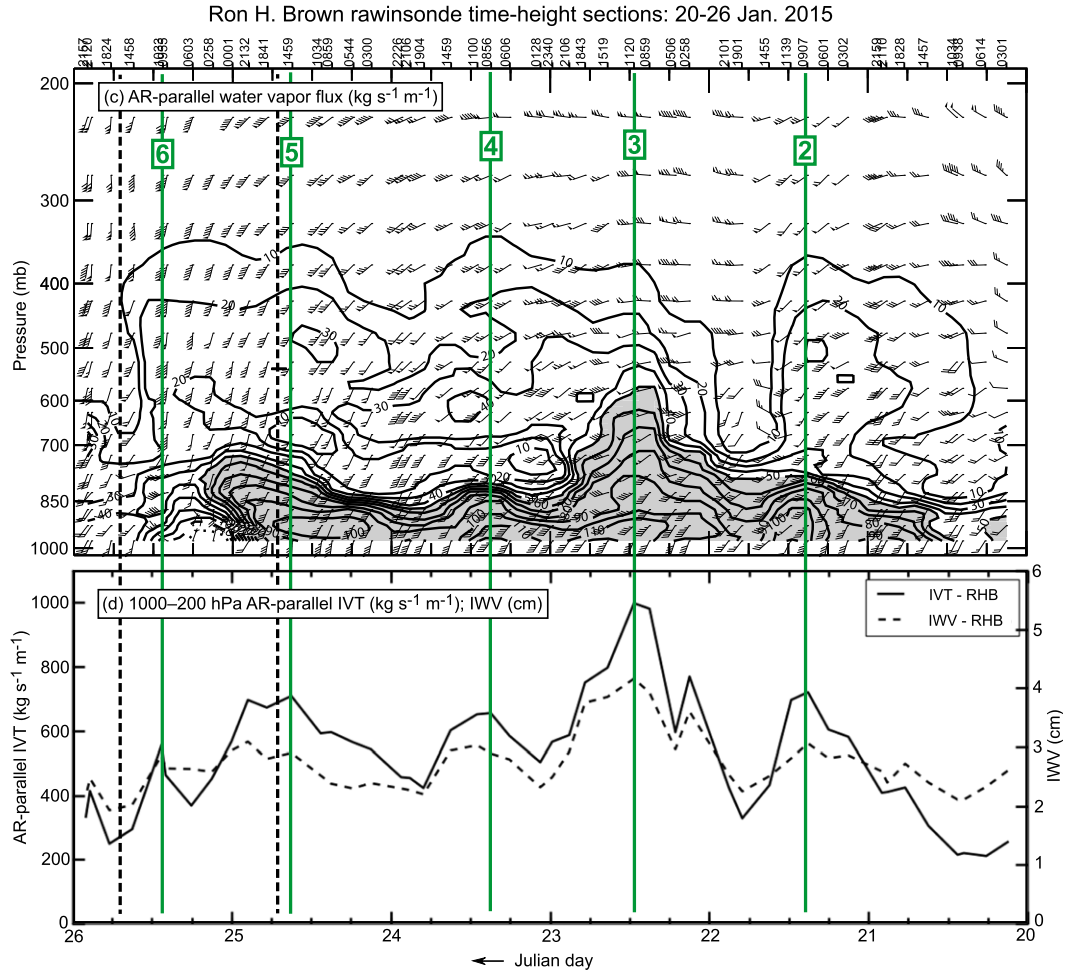Ron H. Brown rawinsonde time-height sections: 20-26 Jan. 2015

FIG. 6. (*Continued*)

southwesterly to westerly flow between 675 and 325 hPa following the passage of frontal wave 2. Warming and moistening ensued with the approach of frontal wave 3, along with the eventual return to southwesterly flow. The warming descended with time to ~850 hPa with the passage of frontal waves 3 and 4. Frontal wave 3 coincided with the deepest vertical penetration of moist RH and the deepest layer of moist-neutral stratification. Deep-layer cooling commenced following the passage of frontal wave 5 and the follow-on front. Below ~850 hPa, thermodynamic conditions in southwesterly flow remained nearly steady state for most of the 6-day period until after ~2200 UTC 24 January with the passage of the front, when θ decreased by 2–4 K, θ_e decreased by 5–8 K, and the flow briefly shifted to northerly. Dry conditions capped this shallow layer, save for the period associated with frontal wave 3 and less so for the period tied to frontal wave 6.

The IVT and IWV time series in Fig. 6d are shown with multiple time series of surface meteorological and SST data from the *RHB* (Fig. 7). The surface flow was southerly until 2200 UTC 24 January, when the front moved across the *RHB* (Fig. 7b). Thereafter, the flow contained a northerly component for ~12 h before reverting to a southerly component. Early in the time series, the magnitude of the southerly flow increased to >8 m s^{-1} at 1600 UTC 20 January shortly after the IVT initially surpassed the minimum AR threshold of 250 kg s^{-1} m^{-1}. The flow exceeded 8 m s^{-1} for 4 days until the frontal passage at 2200 UTC 24 January, after which weaker northerly component flow was observed for 12 h, followed by a return to 8–10 m s^{-1} southerlies. Episodic rainfall occurred during the 6-day period (Fig. 7d). With frontal wave 2, rain rates never exceeded 2.7 mm h^{-1} during individual 5-min periods, and only 1.66 mm fell between 0930 and 1435 UTC 21 January. In contrast, the heaviest rain coincided with frontal wave 3 when the strongest, deepest vapor transports were observed in tandem with deep-layer warming likely associated with warm advection. Between 0235 and 1715 UTC
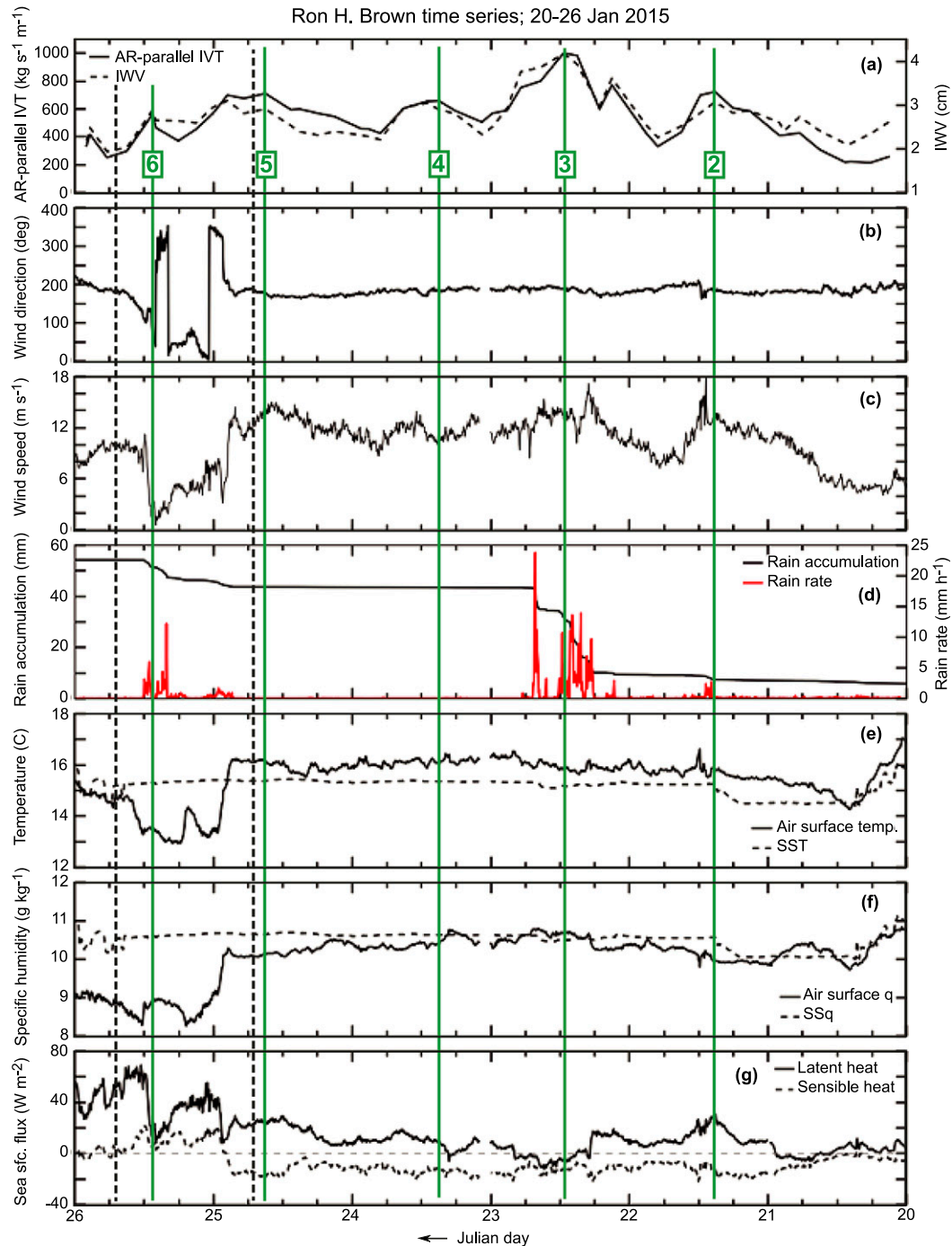
FIG. 7. Time series of data from the *RHB* between 0000 UTC 20 Jan and 0000 UTC 26 Jan 2015: (a) rawinsonde IVT and IWV (as in Fig. 6d); (b),(c) surface wind direction (°) and speed (m s^{-1}); (d) hourly rain rate every 5 min (red; mm h^{-1}) and accumulated rainfall (black; mm); (e) surface air temperature (°C; solid) and SST (°C; dashed); (f) surface air mixing ratio (g kg^{-1}; solid) and sea surface mixing ratio (g kg^{-1}; dashed); and (g) sea surface latent and sensible heat fluxes (W m^{-2}; solid and dashed, respectively; the horizontal thin dashed line marks the zero value of flux). The black and green vertical lines are as in Fig. 6.

22 January, 5-min rain rates were as large as 10–24 mm h^{-1} and 33.85 mm of rain fell. The last period of significant rain occurred between 2030 UTC 24 January and 1240 UTC 25 January (i.e., rain rates as high as 12 mm h^{-1} with 10.49-mm accumulation) with the frontal passage and frontal wave 6.

The *RHB* provided a rare opportunity to collect observations of sea surface sensible and latent heat fluxes in a persistent AR over the open ocean. Toward that end, time series of air surface temperature T_{sfc} and SST (Fig. 7e) are presented, showing T_{sfc} in the AR ranging between 15.2° and 16.5°C and SST between 14.5° and 15.4°C, with $T_{sfc} >$ SST throughout this period. At the leading edge of the front at 2200 UTC 24 January, T_{sfc} decreased abruptly by 3°C in the transition to northerly flow, while the SST remained constant, such that $T_{sfc} <$ SST. Later on 25 January, T_{sfc} rebounded by 2°C when the surface southerlies returned; SST remained constant. Time series of air surface specific humidity q_{sfc} and sea surface saturation specific humidity (SSq; derived from SST) (Fig. 7f) reveal values of 9.9–10.7 g kg^{-1} in the AR, with $q_{sfc} <$ SSq for most of that time. During the frontal passage, q_{sfc} decreased by ~2 g kg^{-1} before rebounding partially, and the deficit of q_{sfc} relative to SSq was maximized. The corresponding fluxes in the AR are as follows (Fig. 7g): $H_S = -5$ to -20 W m^{-2} and $H_L = -10$ to 30 W m^{-2} but mostly positive. The sign of H_S was opposite that observed in an AR over the subtropical North Pacific using aircraft dropsondes (i.e., ~40 W m^{-2}; Neiman et al. 2014b), and the magnitude of upward H_L was less on the *RHB* than from the dropsondes (i.e., ~150 W m^{-2}). The comparative differences in sea surface fluxes between the midlatitude and subtropical locales (38° vs ~24°N) can be accounted for by vastly different SSTs (~15° vs 24°C) and the resulting differences in air–sea temperature contrasts. Following the initial frontal passage at 2200 UTC 24 January when colder air moved over the *RHB*, H_S became mostly positive (as large as 20 W m^{-2}) and H_L became more strongly positive (~10–70 W m^{-2}).

The frontal passage represents the most prominent meteorological transition during this 6-day period on the *RHB*, and it was followed by frontal wave 6 and the subsequent cessation of AR conditions over the ship. A detailed wind-profiler and surface analysis of this important period is presented in Fig. 8. Prior to the leading edge of the frontal passage at 2200 UTC 24 January, strong southwesterly winds extended upward from the surface (10–12 m s^{-1}) to 3 km MSL (30 m s^{-1}), with >20 m s^{-1} AR-parallel flow above 1 km MSL and strong IVT of ~700 kg s^{-1} m^{-1} tied to frontal wave 5. During this period, T_{sfc} of 16°C exceeded SST by ~0.7°C, yielding negative H_S of -15 to -20 W m^{-2}. In
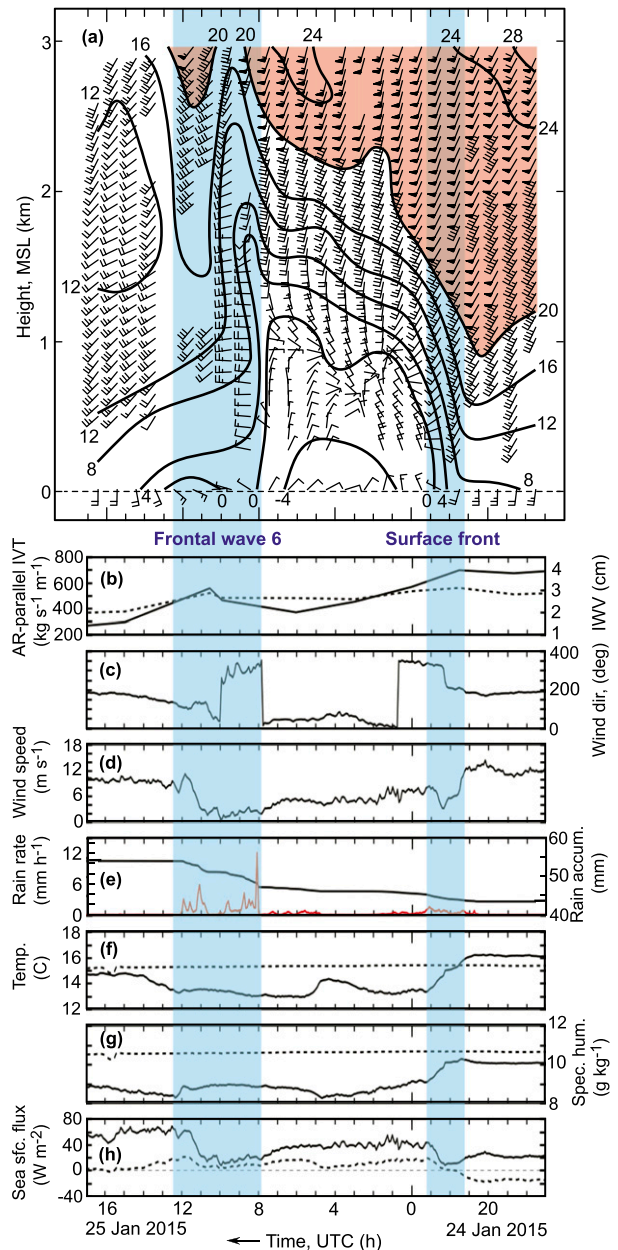

FIG. 8. (a) Time–height section from the *RHB* wind profiler of hourly averaged wind profiles (flags and barbs are as in Fig. 4) and AR-parallel isotachs (black contours, m s^{-1}, directed from 230°) between 1700 UTC 24 Jan and 1700 UTC 25 Jan 2015. (b)–(h) Rawinsonde and surface time series from the *RHB* for the same time span (the variables are the same as in Fig. 7). Blue-shaded boxes with labels denote key meteorological transitions.

contrast, SSq of 10.7 g kg^{-1} exceeded q_{sfc} by ~0.6 g kg^{-1}, yielding positive H_L of 20–30 W m^{-2}. The front was defined by a zone of AR-parallel wind shear temporally ascending from the surface at 2200 UTC 24 January to ~3 km MSL at 0930 UTC 25 January. A shallow layer of northerly component flow below 1 km MSL resided
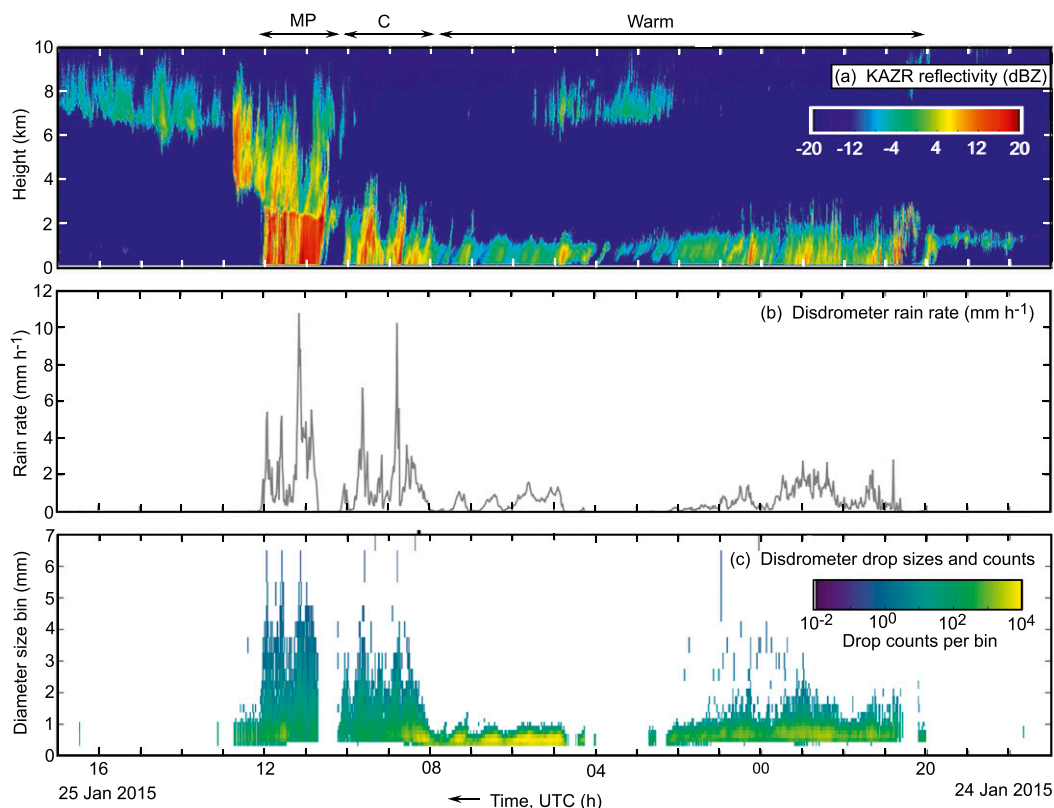
FIG. 9. Microphysics observations from the *RHB* between 1700 UTC 24 Jan and 1700 UTC 25 Jan 2015: (a) time–height section of reflectivity (dB*Z*) from the KAZR radar, (b) time series of instantaneous rain rate (mm h^{-1}; every 60 s) from the Parsivel laser disdrometer, and (c) time series of raindrop sizes (mm) and counts from the disdrometer. The three dominant precipitation periods are labeled: warm, convective (C), and mixed phase (MP). The rain-rate time series in (b) is different than in Fig. 8e, because the time series in (b) is from the Parsivel laser disdrometer with 60-s resolution whereas the time series in Fig. 8e is based on 5-min averages of observations collected from six different rainfall measurement systems.

beneath this shear layer for 9 h before reverting to a southerly component. The surface frontal transition was accompanied by a drop in T_{sfc} and q_{sfc} as described above, a 5.75-h period of light rainfall (i.e., peak rain rate = 1.6 mm h^{-1}; accumulation = 2.63 mm), and a change in sign of H_S along with an increase in magnitude of H_L as described above. During a subsequent transition back to deep-layer southwesterly flow, IVT rebounded briefly to 550 kg s^{-1} m^{-1} with frontal wave 6 before diminishing with the advection of drier and weaker west-southwesterly flow aloft during the eastward migration and decay of the upper-level cyclone. This secondary transition was accompanied by an 8.67-h period of substantial rainfall (i.e., peak rain rate = 12.0 mm h^{-1}; accumulation = 7.86 mm), followed by a prolonged surface pressure rise (not shown).

During the 24-h analysis period highlighted above, the KAZR radar and Parsivel disdrometer captured key microphysical characteristics of the precipitation (Fig. 9). Between 2000 UTC 24 January and 0800 UTC

25 January, temporally uniform (i.e., stratiform) weak echoes ($<\sim$10 dBZ) were confined to a shallow layer far beneath the $\sim$2.5 km MSL melting level (observed several hours later) and generated light rain rates $<$2 mm h^{-1}. The raindrop diameters were small, generally $<$1 mm. Because the precipitation echoes resided beneath the melting level, ice did not play a significant role in its formation. This type of shallow warm rain with small drops was documented previously using vertically pointing S-band profiling (S-PROF) radars (White et al. 2000) along the U.S. West Coast (e.g., Martner et al. 2008; White et al. 2015) and in the southeastern United States (Matrosov et al. 2016). In the West Coast studies, orographic lift generated the warm rain. In the present case, the postfrontal dome of low-level northerly flow (Fig. 8a) provided the shallow lift that generated the warm rain. Between 0800 and 1000 UTC 25 January, as the northerly flow transitioned back to southwesterly with the approach of frontal wave 6, deeper and stronger but intermittent convective echoes
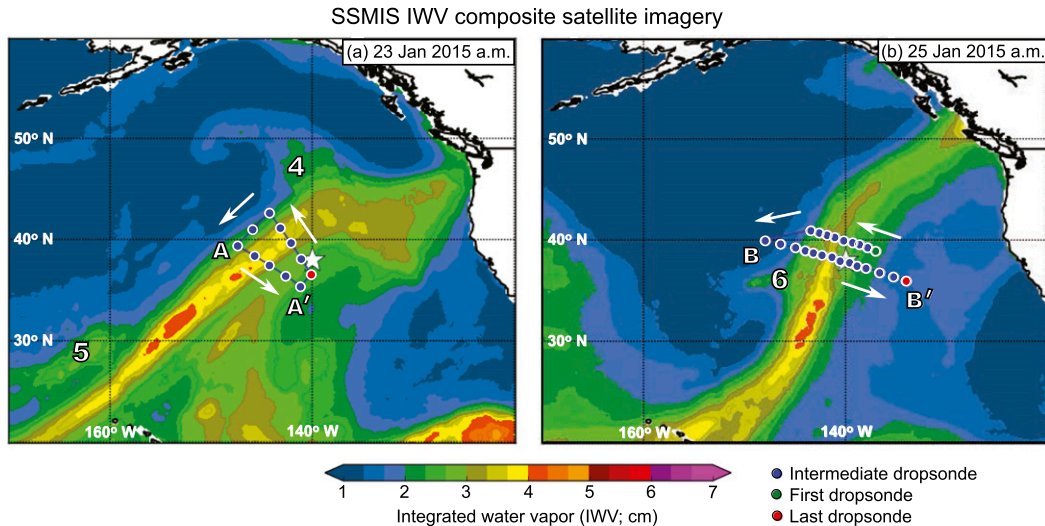
SSMIS IWV composite satellite imagery

FIG. 10. Composite SSMIS satellite imagery of IWV (cm; color scale) constructed from the morning swaths on (a) 23 Jan and (b) 25 Jan 2015. The boldface numbers mark the frontal waves described in the text. The white star in each panel [which is partially obscured in (b) by the dropsonde symbols] denotes the position of the *RHB*. In (a), the positions of the 12 G-IV dropsondes from flight 1 between 2254 UTC 22 Jan and 0139 UTC 23 Jan 2015 are shown (note that the first and last drops occupy the same location). The dropsonde curtain labeled AA′ is the baseline marking the cross section in Fig. 11a. In (b), the positions of the 23 G-IV dropsondes from flight 2 between 2004 and 2303 UTC 24 Jan 2015 are shown. The dropsonde curtain labeled BB′ is the baseline marking the cross sections in Figs. 11b and 12. The directions of the flights are shown with the white arrows.

penetrated upward to the melting level. Rain rates increased to 2–10 mm h^{-1} while the drop size distribution (DSD) broadened, attaining sizes as large as ~2.5 mm. Between 1000 and 1200 UTC during the passage of frontal wave 6, deep stratiform echoes extended up to 8 km MSL, with rain rates comparable to the convective period. The sharp vertical gradient at ~2.5 km MSL marked the melting transition from the weak-echo ice region in mixed-phase clouds aloft to strong-echo (~20 dBZ) rainfall below.[1] The DSD broadened further, with drops as large as ~4 mm, likely contributed by the melted large ice particles. [Similar characteristics were observed previously in deep mixed-phase precipitation from land-based S-PROF radars (e.g., Martner et al. 2008; White et al. 2015; Matrosov et al. 2016).] This period of mixed-phase precipitation is indicative of deep atmospheric forcing, consistent with the observed meteorology. The two earlier periods of rainfall on the *RHB* (on 21 and 22 January) were also associated with deep mixed-phase precipitation (not

shown), and those periods were tied to the passage of frontal waves 2 and 3. The larger droplet number concentrations for the warm clouds relative to the deep mixed-phase clouds (Fig. 9c) are likely related to larger aerosol concentrations at low altitudes. After 1200 UTC 25 January, the strong low-level rain echoes ceased abruptly with the advection of drier air.

b. NOAA G-IV research aircraft

For each G-IV flight, the dropsonde locations are plotted on the composite SSMIS IWV satellite image (Fig. 10) that is closest in time to the dropsondes. The first composite image on the morning (UTC) of 23 January 2015 (Fig. 10a) is composed of satellite retrievals with overpasses at 0242 and 0455 UTC 23 January, respectively, while the AR dropsonde curtain AA′ (i.e., baseline for Fig. 11a) spans the time frame 0038–0127 UTC 23 January. The image on the morning of 25 January (Fig. 10b) is composed of satellite retrievals with overpasses at 0215 and 0430 UTC 25 January, while the AR dropsonde curtain BB′ (i.e., baseline for Figs. 11b and 12) spans the time frame 2127–2303 UTC 25 January and passes directly over the *RHB*. Line AA′ is situated behind frontal wave 4 while BB′ is positioned ahead of frontal wave 6.

The vertical structure of AR-parallel VT along baseline AA′ on 23 January is shown in Fig. 11a. Upright VT > 50 kg s^{-1} m^{-1} extends vertically to ~525 hPa in

---

[1] Because of the radar's short wavelength, a bright band in reflectivity was not observed in this transition. Longer-wavelength radars would have captured the bright band, which is generated by melting precipitation (e.g., Battan 1973) that resides ~200 m below the 0°C level (Stewart et al. 1984; White et al. 2002).
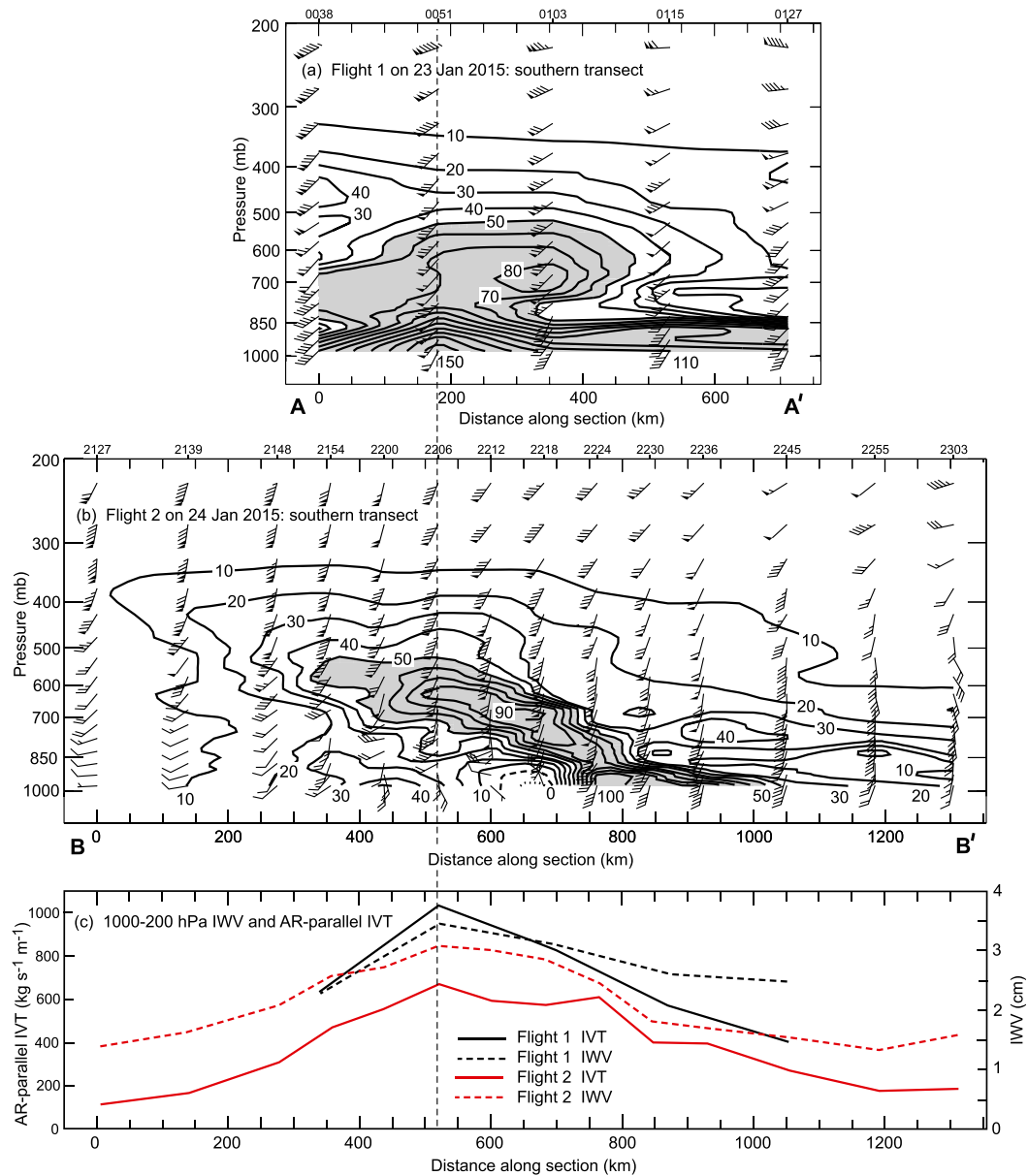
FIG. 11. (a) G-IV dropsonde cross-sectional analysis of AR-parallel horizontal water vapor flux calculated in adjacent 50-hPa layers (kg s^{-1} m^{-1}; directed from 230°; black contours, with shading >50 kg s^{-1} m^{-1}) along AA′ in Fig. 10a, from 0038 to 0127 UTC 23 Jan 2015. (b) G-IV dropsonde cross-sectional analysis of AR-parallel horizontal water vapor flux (kg s^{-1} m^{-1}; directed from 200°; black contours, with shading >50 kg s^{-1} m^{-1}) along BB′ in Fig. 10b, from 2127 to 2303 UTC 24 Jan 2015. In (a) and (b), vertically interpolated wind profiles (every 50 hPa) are plotted (wind flags and barbs are as in Fig. 4), and dropsonde times are shown at the top. (c) G-IV dropsonde traces of 1000–200-hPa AR-parallel IVT (kg s^{-1} m^{-1}; solid) and IWV (cm; dashed) for cross sections AA′ (black) and BB′ (red). Both (a) and (b) are aligned laterally so that their maximum IVT values are collocated in (c); see the vertical dashed black line. In all panels, the distance (km) along the cross section is shown along the bottom.

strong southwesterly flow, with the largest VT below 850 hPa. In the core of the AR, IVT exceeds 1000 kg s^{-1} m^{-1} and IWV approaches 3.5 cm, consistent with the satellite imagery in Fig. 10a. The latter VT cross section on 25 January (Fig. 11b; along baseline BB') also portrays

strong vapor transport in southwesterly flow extending up to ~525 hPa, but with weaker IVT and IWV maxima (650 kg s^{-1} m^{-1} and 3.1 cm, respectively) in the AR core and with different vertical structure. Specifically, the area of VT > 50 kg s^{-1} m^{-1} exhibits a prominent
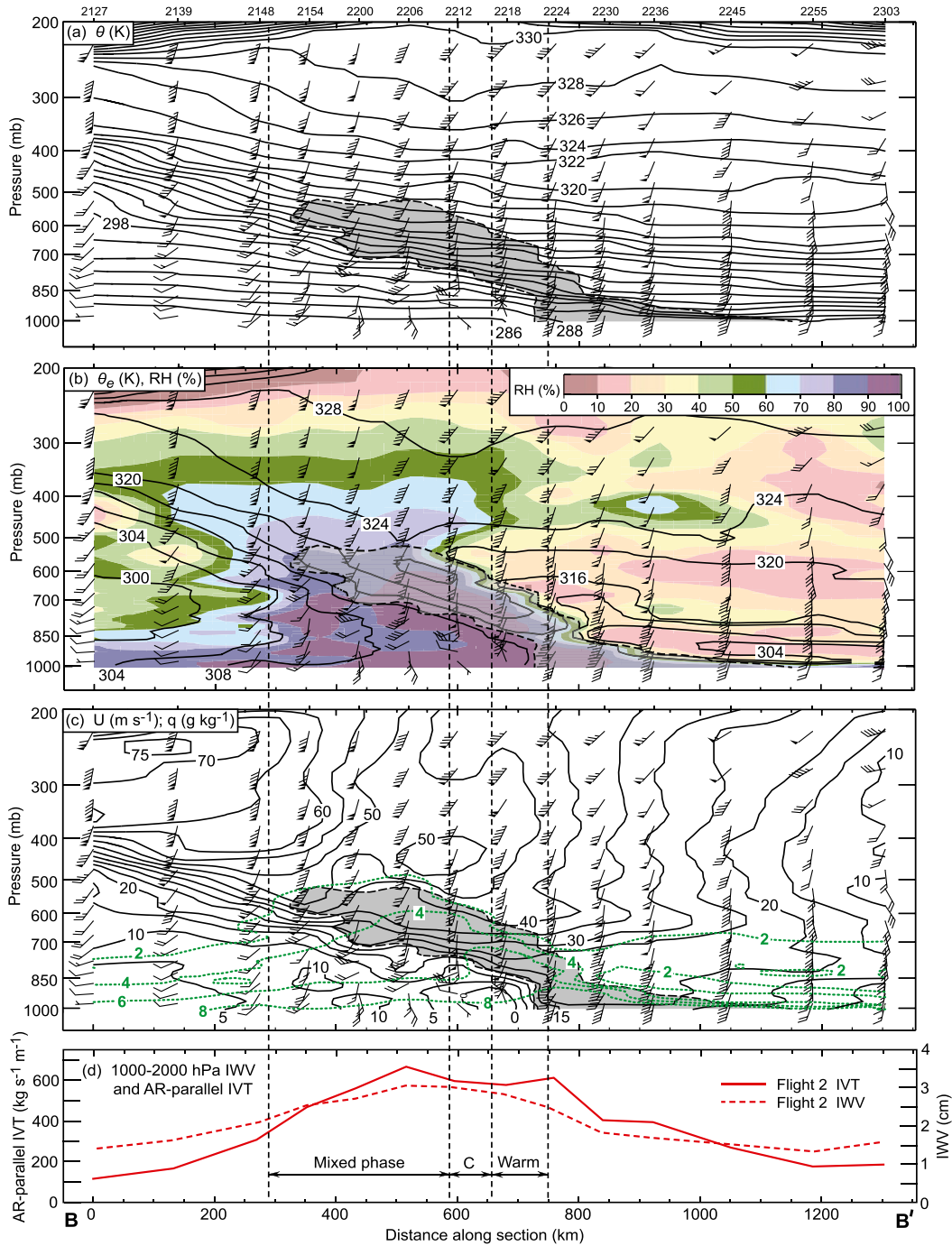
FIG. 12. G-IV dropsonde cross-sectional analyses along BB′ in Fig. 10b, from 2127 to 2303 UTC 24 Jan 2015: (a) θ (K; black contours), (b) θ_e (K; black contours) and relative humidity (%; color scale), and (c) AR-parallel isotachs (m s^{-1}; black contours, directed from 200°) and water vapor specific humidity (g kg^{-1}; green contours). Vertically interpolated wind profiles (every 50 hPa) are plotted (wind flags and barbs are as in Fig. 4), and dropsonde times are shown at the top. AR-parallel horizontal water vapor fluxes >50 kg s^{-1} m^{-1} (from Fig. 11b) are shown in gray shading and bounded with a black dashed line. (d) G-IV dropsonde traces of 1000–200-hPa AR-parallel IVT (kg s^{-1} m^{-1}; solid) and IWV (cm; dashed). The vertical dashed lines bound the three dominant precipitation periods [i.e., warm, convective (C), mixed phase] shown in Fig. 13.

poleward tilt with height, similar to that inferred by the *RHB* rawinsonde time–height section in Fig. 6c. Based on the IWV imagery in Fig. 10, the upright VT plume in the AR cross section on 23 January is located in the trailing cold-frontal region of frontal wave 4 whereas the slantwise plume in the AR cross section on 25 January is situated in the leading warm-frontal region of frontal wave 6. Similar dynamically plausible modulations in the VT field were observed via dropsonde cross sections across an AR in a transient frontal wave over the North Pacific in 2014 (Neiman et al. 2016). The VT cross sections on 23 and 25 January are comparable to their northern counterparts (not shown).

Since the dropsonde transect through the AR at 2127–2303 UTC 25 January intersected the *RHB* when the shallow front was moving across the ship, additional cross-sectional details along baseline BB′ are presented (Figs. 12a–c) in tandem with the previously plotted IVT and IWV along BB′ (Fig. 12d). Cross sections of θ and θ_e (Figs. 12a,b) highlight the collocation of the AR's slantwise VT plume with the sloping dry and moist isentropes of the frontal zone that extend upward to 400 hPa at the northwestern end of the dropsonde curtain. In the AR environment, the region with enhanced RH increases in depth from southeast to northwest within and beneath the sloping frontal zone. Northwest of the AR and front, drier air encroaches above 900 hPa as the low-level flow veers to westerly with the approach of the large-scale trough aloft. A companion cross section of AR-parallel isotachs and specific humidity (Fig. 12c) shows the front accompanied by a well-defined shear zone extending upward from the surface at 2224 UTC 24 January to 400 hPa at the northwestern end of the section. The strongest AR-parallel flow and VT reside on the warm side of the front, and a 75 m s^{-1} south-southwesterly polar jet resides at ~250 hPa near the poleward end of the section. A shallow dome of negative AR-parallel flow is situated immediately on the cold side of the front above the surface. This postfrontal northerly flow was captured in detail by the hourly wind-profiler data aboard the *RHB* (Fig. 8a). The largest values of specific humidity reside on the warm side of the front and at low levels.

The G-IV collected reflectivity and Doppler wind data from the TDR during both flights, although we only present analyses of the precipitating region along cross section BB′ because these analyses (unlike those from AA′) are directly comparable to the *RHB* radar analyses as a result of the close proximity of BB′ with the *RHB* and the AR precipitation. Figure 13a shows a zoomed-in version of Fig. 10b: the baseline BB′ transecting the AR's IWV plume and the dropsonde release times. A plan-view reflectivity analysis at 2 km MSL (Fig. 13b)

depicts precipitation along the flight track from 2149 to 2223 UTC 24 January 2015, with the strongest echoes occurring in the northwestern two-thirds of the rainband (i.e., prior to 2211 UTC). A companion reflectivity cross section (Fig. 13c) reveals that these strong echoes are associated with deep mixed-phase precipitation extending up to >10 km MSL that has a radar brightband melting level situated at 2.0–2.5 km MSL. The weak-echo region in the TDR plan-view analysis between 2215 and 2223 UTC represents the top of a shallow layer of warm rain residing beneath the melting level. Between these two periods of precipitation, from 2211 to 2215 UTC, echoes penetrate above the brightband altitude but do not have brightband characteristics. We refer to this period as convective. The airborne TDR cross-sectional analysis showing three dominant types of precipitation (i.e., mixed phase, convective, and warm) is fully consistent with the KAZR and disdrometer temporal depiction from the *RHB* (Fig. 9). These TDR cross-sectional results are also mapped onto the drop-sonde cross section in Fig. 12 to bolster the rawinsonde-aided meteorological interpretation from the *RHB*. Most significantly, the shallow and light warm rain co-incides with the initial surface frontal passage and trailing zone of shallow postfrontal northerly flow, while the deep and heavy mixed-phase precipitation coincides with the strongest IVT and IWV in the AR core during the frontal passage aloft with frontal wave 6. The brightband exhibits a poleward decrease in altitude from 2.5 to 2.0 km across the front aloft.

5. Conclusions

This study describes the structure and evolution of a long-lived AR over the northeastern Pacific on 20–25 January 2015 using a unique suite of mobile observing platforms deployed on NOAA's R/V *RHB* and G-IV research aircraft during the CalWater-2015 field campaign. This is the first AR study of its kind, analyzing diverse observations collected aboard the *RHB* and subsequently integrating these shipborne analyses with airborne analyses generated using data collected from the G-IV. As such, this study provides new observational insights into ARs over the open ocean. During the multiple days of continuous AR conditions, significant spatiotemporal variability of the thermodynamic, kinematic, and precipitation characteristics were observed by the myriad observing systems aboard the *RHB* and G-IV. Although the AR remained far offshore of the U.S. West Coast, it made landfall across western British Columbia where heavy precipitation fell in conjunction with high melting levels, resulting in localized flooding.
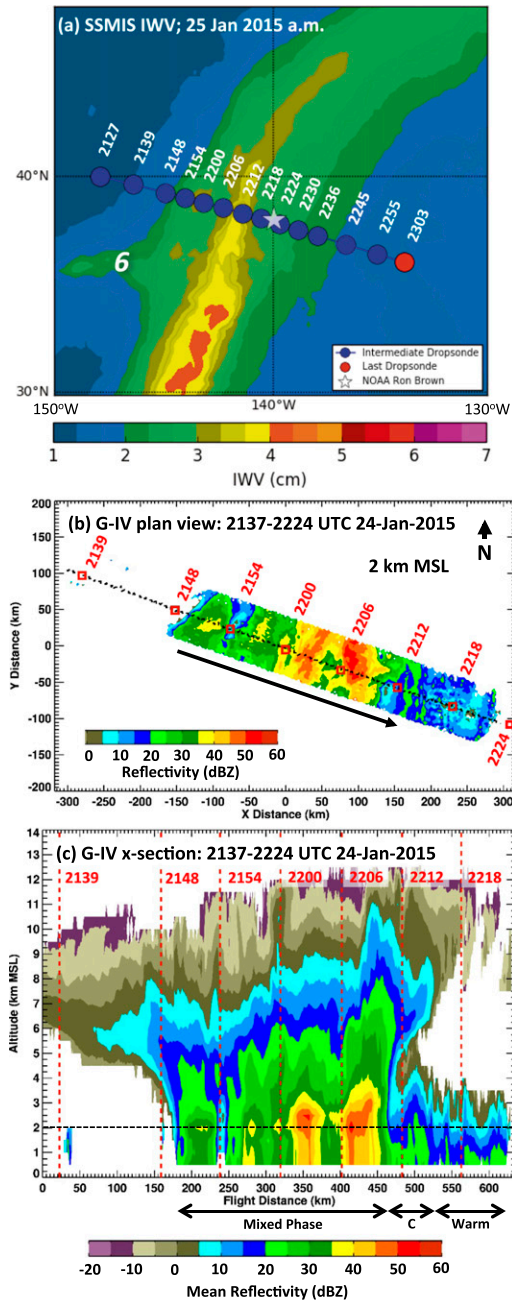
FIG. 13. (a) Composite SSMIS satellite imagery of IWV (cm) on the morning of 25 Jan 2015, as in Fig. 10b. The G-IV dropsonde release times between 2127 and 2303 UTC 24 Jan 2015 are labeled. (b),(c) Decluttered and Cartesian-gridded radar reflectivity (dBZ) analyses from the NOAA G-IV TDR aft scans between 2137 and 2224 UTC 24 Jan 2015. The plan-view perspective in (b) is valid at 2 km MSL. In (b), the flight track is portrayed with a black dotted line, and the dropsonde positions are shown with red squares and labeled with their release times (UTC) on 24 Jan. The cross-sectional perspective in (c) is along the flight track shown in (b), and the reflectivity represents a ±9-km cross-track average. The horizontal black dashed line resides at the altitude of the 2 km MSL plan-view analysis, and the vertical red dashed lines mark the dropsonde positions (labeled with their release times). The three dominant precipitation periods are labeled: warm, convective (C), and mixed phase.

SSMIS satellite observations and gridded CFSR reanalysis diagnostics (Figs. 1–5) provided synoptic-scale context for this 6-day case study. Throughout the event, an upper-level trough and ridge persisted over the central North Pacific Ocean and U.S. West Coast, respectively. Between these two synoptic-scale circulations, a warm and moist southwesterly airstream within a quasi-stationary AR was situated on the equatorward side of a frontal baroclinic zone extending from the subtropics to British Columbia. A series of six transient frontal waves modulated the front and AR, ultimately resulting in oscillatory motions about the front and AR's mean position. Toward the end of the study period, the front and AR began moving eastward across the *RHB* and subsequently weakened in response to the eastward migration and weakening of the upper-level synoptic-scale trough.

To facilitate the collection of atmospheric and oceanographic data from the impressive array of shipborne instrumentation over the data-sparse Pacific for the 6-day duration of this study, the *RHB* anchored in the quasi-stationary path of the AR. A total of 47 rawinsondes launched from the *RHB* provided a comprehensive thermodynamic and kinematic depiction of the AR, including an upward intrusion of strong water vapor transport in the low-level moist southwesterly flow and an associated maximum in IVT and IWV during the passage of frontal waves 2–6 (Fig. 6). Light rainfall occurred with frontal wave 2, while the heaviest rain coincided with frontal wave 3 (Fig. 7) during the strongest, deepest vapor transports in a deep layer of warm advection. The last episode of rain occurred with the frontal passage and frontal wave 6; this period represents the most prominent meteorological transition of the case study aboard the *RHB*. A detailed analysis from the collocated 1290-MHz wind profiler (Fig. 8) showed an abrupt frontal transition from southwesterly to northerly flow below 1 km MSL coinciding with a decrease in surface temperature (specific humidity) of 3°C (2 g kg^{-1}). Low-level southwesterly flow subsequently descended from aloft with frontal wave 6. Concurrent and collocated observations from the KAZR cloud radar and disdrometer (Fig. 9) captured key microphysical characteristics of the precipitation. The shallow postfrontal northerly flow was accompanied by low-intensity warm rain with small drops generated below the melting level, quite likely in response to weak, low-level frontal uplift. The rain became heavier with frontal wave 6 and transitioned to a deeper mixed-phase character possessing a melting level at 2.0–2.5 km MSL and larger raindrops.

The *RHB* provided a rare opportunity to collect continuous observations of sea surface sensible and latent heat fluxes in a persistent AR over the open ocean

in the extratropics (Figs. 7 and 8). For four consecutive days leading up to the final cold-frontal passage, sensible heat fluxes in the AR were modestly negative (from -5 to $-20\,\mathrm{W\,m}^{-2}$) while latent heat fluxes were mostly positive (as large as $30\,\mathrm{W\,m}^{-2}$). Once colder and drier air advected over the *RHB* behind the advancing front, sensible heat fluxes became positive (as large as $20\,\mathrm{W\,m}^{-2}$) and latent fluxes became more strongly positive (up to $70\,\mathrm{W\,m}^{-2}$). Although a prior study by Neiman et al. (2014b) was the first to present air–sea flux measurements in an AR, it was only a snapshot from a box pattern of dropsondes estimated from a bulk flux method. Using a budget analysis, that study documented boundary layer moistening in the AR near Hawaii due, in part, to evaporation from the ocean surface. Using a more rigorous budget analysis in an AR farther north over the extratropical Pacific, Cordeira et al. (2013) also showed AR moistening due to evaporation from the ocean surface, although that study was based on re-analysis data. Since the exchange of sensible and latent heat between the ocean and the atmosphere can modulate storm structure and intensity (e.g., Fleagle and Nuss 1985; Bond and Fleagle 1988; Kelly et al. 2010) and provide additional water vapor to enhance precipitation with AR landfalls, air–sea flux observations provided by the *RHB* in this and future studies can ultimately offer key observational insights into the evolution of ARs. In the present case, an observed maximum latent heat flux of $30\,\mathrm{W\,m}^{-2}$ in the AR corresponds to a daily increase in IWV of 1.1 mm. The average rain rate during the $\sim$4-day AR period on the *RHB* (Fig. 7d) was a much larger $9.7\,\mathrm{mm\,day}^{-1}$. Given that the IWV in the AR core did not change appreciably during this period (Fig. 1), horizontal convergence rather than ocean surface evaporation represented the dominant water vapor source. Also, it is plausible that enhanced low-level flow in the core of the frontal waves (which were positioned mostly west of the *RHB*; see Figs. 1 and 3) provided a mechanism for infusing additional water vapor from the ocean surface into the AR, which, ultimately, rained out.

The G-IV analyses presented in this study (Figs. 11–13) add to the growing knowledge base gleaned from previous overocean airborne AR studies (e.g., Ralph et al. 2004, 2005, 2011; Neiman et al. 2014b, 2016). In addition, this is the first AR study that coordinated a research ship and an aircraft that flew directly over the ship. The G-IV flew two missions, each with two dropsonde transects across the AR, during which the tail-mounted Doppler radar gathered precipitation data. The dropsonde and radar spatial analyses complemented the rawinsonde and radar temporal depictions of the AR from the *RHB*. Fortuitously, the first flight penetrated the cold-frontal region of frontal wave 4 and captured an upright vapor

transport plume in the AR, whereas the second flight cut across the warm-frontal region of frontal wave 6 and documented a slantwise vapor transport plume sloping poleward with increasing height. Similar dynamically plausible modulations in the VT field were observed via dropsonde cross sections across an AR in a transient frontal wave over the North Pacific in 2014 (Neiman et al. 2016).

The coordinated observations from the multiple observing platforms over the northeastern Pacific Ocean provided important new perspectives on the structure and evolution of ARs. Ultimately, when these results are integrated into the modeling framework (beyond the scope of this paper), they can improve AR forecasts, which have been shown to be deficient in a study by Wick et al. (2013) that compared forecasts of AR attributes in five operational ensemble systems with SSMIS IWV satellite imagery of ARs over the northeastern Pacific and west coast of North America for three cool seasons (October–March) between 2008 and 2011. Although the models did a reasonable job forecasting the occurrence and core IWV content of ARs out to 10 days, the width of the ARs was overpredicted except for the finest-resolution (i.e., 0.5° latitude–longitude) model. The implication here is that relatively coarse-resolution climate models may have difficulty capturing the details of ARs. The study also reveals that forecasting AR landfalls can be problematic, especially for longer lead times when positional errors increased to $\sim$800 km for 10-day forecasts. Accurate forecasting of the location, timing, and duration of ARs at landfall can be crucial in both the short term such as for issuing hydrometeorology-related warnings and in the multiday time frame for forecast-based dam operations. This accuracy at landfall can be impacted significantly by the type of frontal waves that were documented in the present study.

comments offered by Darren Jackson and Dr. James Wilczak of NOAA/PSD and by three anonymous reviewers for *Monthly Weather Review*.

APPENDIX

Calculating Sea Surface Sensible and Latent Heat Fluxes

Meteorological and SST data aboard the *RHB* were used to calculate sea surface sensible and latent heat fluxes. The turbulent flux F_x of some constituent x in the atmosphere can be represented as

$$F_x = \overline{w'x'}, \tag{A1}$$

where the prime implies a fluctuating or turbulent component, w the vertical velocity, and the overbar represents a time or space average. For example, the sensible and latent heat fluxes (H_S and H_L, respectively) are

$$H_S = \rho_a C_p \overline{w'T'} \quad \text{and} \tag{A2}$$

$$H_L = \rho_a L_e \overline{w'q'}, \tag{A3}$$

where ρ_a is the air density, C_p the specific heat of dry air, L_e the latent heat of vaporization of water, T' are temperature fluctuations, and q' are fluctuations of specific humidity. Fluxes are typically estimated using three methods: bulk, inertial-dissipation (ID), and direct covariance (Fairall et al. 1996). The first two methods rely on empirical coefficients and similarity theory while the third method is a direct application of Eqs. (A2) and (A3). The covariance method yields an unbiased estimate of the flux within the accuracy of the sensors and various corrections (principally ship motion). The time series of w', T', and q' were obtained from the sonic anemometer and fast response infrared absorption instrument. For the turbulent velocities, a number of complications arise from measurements with a ship. First, the raw time series of the three velocity components from the sonic anemometer are rotated from the tilted ship frame to an untilted ship frame (Edson and Fairall 1998). A flow distortion correction is applied to remove velocity errors caused by the ship's structure (based on comparisons with the *RHB* and buoys). Finally, the velocities are transformed to an earth (i.e., east, north) frame and mean ship motion is removed. This yields the fast time series of velocity components, including w'. The time series of w' is multiplied with the time series of T' and q' and averaged; 5-min averages are used. The 5-min averages yield noisy covariance turbulent flux measurements, although the same short averaging periods for the nonturbulent measurements are important in documenting abrupt changes in frontal regions. For CalWater-2015, the fluxes were estimated using all three methods. For bulk fluxes, we used the COARE algorithm, version 3.0 (Edson et al. 2013), which yielded a good fit to the covariance fluxes for CalWater-2015 [for a discussion of the accuracy of the covariance method, see Fairall et al. (2003)]. Because of this good agreement, and the fact that the bulk technique was less noisy than the covariance technique for the 5-min averages, we show the results from the bulk methodology for calculating sea surface sensible and latent heat fluxes.

REFERENCES

Ault, A. P., C. R. Williams, A. B. White, P. J. Neiman, J. M. Creamean, C. J. Gaston, F. M. Ralph, and K. A. Prather, 2011: Detection of Asian dust in California orographic precipitation. *J. Geophys. Res.*, **116**, D16205, doi:10.1029/2010JD015351.

Battan, L. J., 1973: *Radar Observations of the Atmosphere*. University of Chicago Press, 279 pp.

Bond, N. A., and R. G. Fleagle, 1988: Prefrontal and postfrontal boundary layer processes over the ocean. *Mon. Wea. Rev.*, **116**, 1257–1273, doi:10.1175/1520-0493(1988)116<1257:PAPBLP>2.0.CO;2.

Cordeira, J. M., F. M. Ralph, and B. J. Moore, 2013: The development and evolution of two atmospheric rivers in proximity to western North Pacific tropical cyclones in October 2010. *Mon. Wea. Rev.*, **141**, 4234–4255, doi:10.1175/MWR-D-13-00019.1.

Creamean, J. M., and Coauthors, 2013: Dust and biological aerosols from the Sahara and Asia influence precipitation in the western U.S. *Science*, **339**, 1572–1578, doi:10.1126/science.1227279.

——, A. P. Ault, A. B. White, P. J. Neiman, F. M. Ralph, and K. A. Prather, 2015: Interannual variations in aerosol sources and their impacts on orographic precipitation over California's central Sierra Nevada. *Atmos. Chem. Phys.*, **15**, 6535–6548, doi:10.5194/acp-15-6535-2015.

Dettinger, M. D., 2004: Fifty-two years of "pineapple-express" storms across the west coast of North America. California Energy Commission Rep. CEC-500-2005-004, Public Interest Energy Research Program, 15 pp. [Available online at http://www.energy.ca.gov/2005publications/CEC-500-2005-004/CEC-500-2005-004.PDF.]

——, F. M. Ralph, T. Das, P. J. Neiman, and D. Cayan, 2011: Atmospheric rivers, floods, and the water resources of California. *Water*, **3**, 445–478, doi:10.3390/w3020445.

Edson, J. B., and C. W. Fairall, 1998: Similarity relationships in the marine atmospheric surface layer for terms in the TKE and scalar variance budgets. *J. Atmos. Sci.*, **55**, 2311–2338, doi:10.1175/1520-0469(1998)055<2311:SRITMA>2.0.CO;2.

——, and Coauthors, 2013: On the exchange of momentum over the open ocean. *J. Phys. Oceanogr.*, **43**, 1589–1610, doi:10.1175/JPO-D-12-0173.1.

Fairall, C. W., E. F. Bradley, D. P. Rogers, J. B. Edson, and G. S. Young, 1996: Bulk parameterization of air-sea fluxes for Tropical Ocean-Global Atmosphere Coupled-Ocean Atmosphere Response Experiment. *J. Geophys. Res.*, **101**, 3747–3767, doi:10.1029/95JC03205.

——, ——, J. E. Hare, A. A. Grachev, and J. B. Edson, 2003: Bulk parameterization of air–sea fluxes: Updates and verification for the COARE algorithm. *J. Climate*, **16**, 571–591, doi:10.1175/1520-0442(2003)016<0571:BPOASF>2.0.CO;2.

Fleagle, R. G., and W. A. Nuss, 1985: The distribution of surface fluxes and boundary layer divergence in midlatitude ocean storms. *J. Atmos. Sci.*, **42**, 784–799, doi:10.1175/1520-0469(1985)042<0784:TDOSFA>2.0.CO;2.

Guan, B., D. E. Waliser, N. P. Molotch, E. J. Fetzer, and P. J. Neiman, 2012: Does the Madden–Julian oscillation influence wintertime atmospheric rivers and snowpack in the Sierra Nevada? *Mon. Wea. Rev.*, **140**, 325–342, doi:10.1175/MWR-D-11-00087.1.

——, N. P. Molotch, D. E. Waliser, E. J. Fetzer, and P. J. Neiman, 2013: The 2010/11 snow season in California's Sierra Nevada: Role of atmospheric rivers and modes of large-scale variability. *Water Resour. Res.*, **49**, 6731–6743, doi:10.1002/wrcr.20537.

Karstens, U., C. Simmer, and E. Ruprect, 1994: Remote sensing of cloud liquid water. *Meteor. Atmos. Phys.*, **54**, 157–171, doi:10.1007/BF01030057.

Kelly, K. A., R. J. Small, R. M. Samuelson, B. Qiu, T. M. Joyce, Y.-O. Kwon, and M. F. Cronin, 2010: Western boundary currents and frontal air–sea interaction: Gulf Stream and Kuroshio extension. *J. Climate*, **23**, 5644–5667, doi:10.1175/2010JCLI3346.1.

Kingsmill, D. E., P. J. Neiman, B. J. Moore, M. Hughes, S. E. Yuter, and F. M. Ralph, 2013: Kinematic and thermodynamic structures of Sierra barrier jets and overrunning atmospheric rivers during a landfalling winter storm in northern California. *Mon. Wea. Rev.*, **141**, 2015–2036, doi:10.1175/MWR-D-12-00277.1.

Kunkee, D., G. A. Poe, D. Boucher, S. Swadley, Y. Hong, J. Wessel, and E. Uliana, 2008: Design and evaluation of the first Special Sensor Microwave Imager/Sounder (SSMIS). *IEEE Trans. Geosci. Remote Sens.*, **46**, 863–883, doi:10.1109/TGRS.2008.917980.

Lavers, D. A., and G. Villarini, 2013: The nexus between atmospheric rivers and extreme precipitation across Europe. *Geophys. Res. Lett.*, **40**, 3259–3264, doi:10.1002/grl.50636.

——, R. P. Allan, E. F. Wood, G. Villarini, D. J. Brayshaw, and A. J. Wade, 2011: Floods in Britain are connected with atmospheric rivers. *Geophys. Res. Lett.*, **38**, L23803, doi:10.1029/2011GL049783.

Leung, L. R., 2016: ARM Cloud-Aerosol-Precipitation Experiment (ACAPEX) field campaign report. Department of Energy Tech. Rep. DOE/SC-ARM-16-012, 24 pp. [Available online at https://www.arm.gov/publications/programdocs/doe-sc-arm-16-012.pdf.]

Löffler-Mang, M., and J. Joss, 2000: An optical disdrometer for measuring size and velocity of hydrometeors. *J. Atmos. Oceanic Technol.*, **17**, 130–139, doi:10.1175/1520-0426(2000)017<0130:AODFMS>2.0.CO;2.

Martin, T., P. Muradyan, and R. Coulter, 2014: Spectra from 1290-MHz Beam-Steered Radar Wind Profiler (BSRWP) operating in low precipitation mode. Atmospheric Radiation Measurement Archive, Oak Ridge National Laboratory, Oak Ridge, TN, accessed January 2016, doi:10.5439/1256319.

Martner, B. E., S. E. Yuter, A. B. White, S. Y. Matrosov, D. E. Kingsmill, and F. M. Ralph, 2008: Raindrop size distributions and rain characteristics in California coastal rainfall for periods with and without a radar bright band. *J. Hydrometeor.*, **9**, 408–425, doi:10.1175/2007JHM924.1.

Matrosov, S. Y., R. Cifelli, P. J. Neiman, and A. B. White, 2016: Radar rain-rate estimators and their variability due to rainfall types: An assessment based on Hydrometeorology Testbed data from the southeastern United States. *J. Appl. Meteor. Climatol.*, **55**, 1345–1358, doi:10.1175/JAMC-D-15-0284.1.

Nalli, N. R., and Coauthors, 2016: Satellite sounder observations of contrasting tropospheric moisture transport regimes: Saharan air layers, Hadley cells, and atmospheric rivers. *J. Hydrometeor.*, **17**, 2997–3006, doi:10.1175/JHM-D-16-0163.1.

Neiman, P. J., F. M. Ralph, G. A. Wick, Y.-H. Kuo, T.-K. Wee, Z. Ma, G. H. Taylor, and M. D. Dettinger, 2008a: Diagnosis of an intense atmospheric river impacting the Pacific Northwest: Storm summary and offshore vertical structure observed with COSMIC satellite retrievals. *Mon. Wea. Rev.*, **136**, 4398–4420, doi:10.1175/2008MWR2550.1.

——, ——, ——, J. Lundquist, and M. D. Dettinger, 2008b: Meteorological characteristics and overland precipitation impacts of atmospheric rivers affecting the west coast of North America based on eight years of SSM/I satellite observations. *J. Hydrometeor.*, **9**, 22–47, doi:10.1175/2007JHM855.1.

——, L. J. Schick, F. M. Ralph, M. Hughes, and G. A. Wick, 2011: Flooding in western Washington: The connection to atmospheric rivers. *J. Hydrometeor.*, **12**, 1337–1358, doi:10.1175/2011JHM1358.1.

——, M. Hughes, B. J. Moore, F. M. Ralph, and E. S. Sukovich, 2013a: Sierra barrier jets, atmospheric rivers, and precipitation characteristics in northern California: A composite perspective based on a network of wind profilers. *Mon. Wea. Rev.*, **141**, 4211–4233, doi:10.1175/MWR-D-13-00112.1.

——, F. M. Ralph, B. J. Moore, M. Hughes, K. M. Mahoney, J. Cordeira, and M. D. Dettinger, 2013b: The landfall and inland penetration of a flood-producing atmospheric river in Arizona. Part I: Observed synoptic-scale, orographic, and hydrometeorological characteristics. *J. Hydrometeor.*, **14**, 460–484, doi:10.1175/JHM-D-12-0101.1.

——, ——, and ——, 2014a: The regional influence of an intense barrier jet and atmospheric river on orographic precipitation in northern California: A case study. *J. Hydrometeor.*, **15**, 1419–1439, doi:10.1175/JHM-D-13-0183.1.

——, G. A. Wick, B. J. Moore, F. M. Ralph, J. R. Spackman, and B. Ward, 2014b: An airborne study of an atmospheric river over the subtropical Pacific during WISPAR: Dropsonde budget-box diagnostics, and precipitation impacts in Hawaii. *Mon. Wea. Rev.*, **142**, 3199–3223, doi:10.1175/MWR-D-13-00383.1.

——, B. J. Moore, A. B. White, G. A. Wick, J. Aikins, D. L. Jackson, J. R. Spackman, and F. M. Ralph, 2016: An airborne and ground-based study of a long-lived and intense atmospheric river with mesoscale frontal waves impacting California during CalWater2-2014. *Mon. Wea. Rev.*, **144**, 1115–1144, doi:10.1175/MWR-D-15-0319.1.

Ralph, F. M., and M. D. Dettinger, 2012: Historical and national perspectives on extreme West Coast precipitation associated with atmospheric rivers during December 2010. *Bull. Amer. Meteor. Soc.*, **93**, 783–790, doi:10.1175/BAMS-D-11-00188.1.

——, P. J. Neiman, D. E. Kingsmill, P. O. G. Persson, A. B. White, E. T. Strem, E. D. Andrews, and R. C. Antweiler, 2003: The impact of a prominent rain shadow on flooding in California's Santa Cruz Mountains: A CALJET case study and sensitivity to the ENSO cycle. *J. Hydrometeor.*, **4**, 1243–1264, doi:10.1175/1525-7541(2003)004<1243:TIOAPR>2.0.CO;2.

——, ——, and G. A. Wick, 2004: Satellite and CALJET aircraft observations of atmospheric rivers over the eastern North Pacific Ocean during the winter of 1997/98. *Mon. Wea. Rev.*, **132**, 1721–1745, doi:10.1175/1520-0493(2004)132<1721:SACAOO>2.0.CO;2.

——, ——, and R. Rotunno, 2005: Dropsonde observations in low-level jets over the northeastern Pacific Ocean from CALJET-1998 and PACJET-2001: Mean vertical-profile and atmospheric-river characteristics. *Mon. Wea. Rev.*, **133**, 889–910, doi:10.1175/MWR2896.1.

——, ——, G. A. Wick, S. I. Gutman, M. D. Dettinger, D. R. Cayan, and A. B. White, 2006: Flooding on California's Russian River: The role of atmospheric rivers. *Geophys. Res. Lett.*, **33**, L13801, doi:10.1029/2006GL026689.

——, ——, G. N. Kiladis, K. Weickmann, and D. M. Reynolds, 2011: A multiscale observational case study of a Pacific atmospheric river exhibiting tropical–extratropical connections and a mesoscale frontal wave. *Mon. Wea. Rev.*, **139**, 1169–1189, doi:10.1175/2010MWR3596.1.

——, and Coauthors, 2013: The emergence of weather-related testbeds linking research and forecasting operations. *Bull. Amer. Meteor. Soc.*, **94**, 1187–1211, doi:10.1175/BAMS-D-12-00080.1.

——, and Coauthors, 2016: CalWater field studies designed to quantify the roles of atmospheric rivers and aerosols in modulating U.S. West Coast precipitation in a changing climate. *Bull. Amer. Meteor. Soc.*, **97**, 1209–1228, doi:10.1175/BAMS-D-14-00043.1.

Rutz, J. J., W. J. Steenburgh, and F. M. Ralph, 2014: Climatological characteristics of atmospheric rivers and their inland penetration over the western United States. *Mon. Wea. Rev.*, **142**, 905–921, doi:10.1175/MWR-D-13-00168.1.

Saha, S., and Coauthors, 2010: The NCEP Climate Forecast System Reanalysis. *Bull. Amer. Meteor. Soc.*, **91**, 1015–1057, doi:10.1175/2010BAMS3001.1.

Smith, B. L., S. E. Yuter, P. J. Neiman, and D. E. Kingsmill, 2010: Water vapor fluxes and orographic precipitation over northern California associated with a land-falling atmospheric river. *Mon. Wea. Rev.*, **138**, 74–100, doi:10.1175/2009MWR2939.1.

Stewart, R. E., J. D. Marwitz, J. C. Pace, and R. E. Carbone, 1984: Characteristics through the melting layer of stratiform clouds. *J. Atmos. Sci.*, **41**, 3227–3237, doi:10.1175/1520-0469(1984)041<3227:CTTMLO>2.0.CO;2.

Stohl, A., C. Forster, and H. Sodemann, 2008: Remote sources of water vapor forming precipitation on the Norwegian west coast at 60°N–A tale of hurricanes and an atmospheric river. *J. Geophys. Res.*, **113**, D05102, doi:10.1029:2007JD009006.

Viale, M., and M. N. Nuñez, 2011: Climatology of winter orographic precipitation over the subtropical central Andes and associated synoptic and regional characteristics. *J. Hydrometeor.*, **12**, 481–507, doi:10.1175/2010JHM1284.1.

Weber, B. L., D. B. Wuertz, D. C. Welsh, and R. McPeek, 1993: Quality controls for profiler measurements of winds and RASS temperatures. *J. Atmos. Oceanic Technol.*, **10**, 452–464, doi:10.1175/1520-0426(1993)010<0452:QCFPMO>2.0.CO;2.

Wentz, F. J., 1995: The intercomparison of 53 SSM/I water vapor algorithms. Remote Sensing Systems Tech. Rep., Santa Rosa, CA, 19 pp.

White, A. B., J. R. Jordan, B. E. Martner, F. M. Ralph, and B. W. Bartram, 2000: Extending the dynamic range of an S-band radar for cloud and precipitation studies. *J. Atmos. Oceanic Technol.*, **17**, 1226–1234, doi:10.1175/1520-0426(2000)017<1226:ETDROA>2.0.CO;2.

——, D. J. Gottas, E. Strem, F. M. Ralph, and P. J. Neiman, 2002: An automated brightband height detection algorithm for use with Doppler radar vertical spectral moments. *J. Atmos. Oceanic Technol.*, **19**, 687–697, doi:10.1175/1520-0426(2002)019<0687:AABHDA>2.0.CO;2.

——, and Coauthors, 2013: A twenty-first-century California observing network for monitoring extreme weather events. *J. Atmos. Oceanic Technol.*, **30**, 1585–1603, doi:10.1175/JTECH-D-12-00217.1.

——, P. J. Neiman, J. M. Creamean, T. Coleman, F. M. Ralph, and K. A. Prather, 2015: The impacts of California's San Francisco Bay Area gap on precipitation observed in the Sierra Nevada during HMT and CalWater. *J. Hydrometeor.*, **16**, 1048–1069, doi:10.1175/JHM-D-14-0160.1.

Wick, G. A., P. J. Neiman, F. M. Ralph, and T. M. Hamill, 2013: Evaluation of forecasts of the water vapor signature of atmospheric rivers in operational numerical weather prediction models. *Wea. Forecasting*, **28**, 1337–1352, doi:10.1175/WAF-D-13-00025.1.

Widener, K., N. Bharadwaj, and K. Johnson, 2012: Ka-Band ARM Zenith Radar (KAZR). Department of Energy Tech. Rep. DOE/SC-ARM/TR-106, 25 pp. [Available online at https://www.arm.gov/publications/tech_reports/handbooks/kazr_handbook.pdf.]

Zhu, Y., and R. E. Newell, 1998: A proposed algorithm for moisture fluxes from atmospheric rivers. *Mon. Wea. Rev.*, **126**, 725–735, doi:10.1175/1520-0493(1998)126<0725:APAFMF>2.0.CO;2.